Acoustics of Jet Surface Interaction – Scrubbing Noise

Abbas Khavaran
Vantage Partners, LLC.
NASA Glenn Research Center, Cleveland, OH 44135, USA
Abbas.Khavaran-1@nasa.gov

Abstract

Concepts envisioned for the future of civil air transport consist of unconventional propulsion systems in the close proximity to the structure or embedded in the airframe. While such integrated systems are intended to shield noise from the community, they also introduce new sources of sound. Sound generation due to interaction of a jet flow past a nearby solid surface is investigated here using the generalized acoustic analogy theory. The analysis applies to the boundary layer noise generated at and near a wall, and excludes the scattered noise component that is produced at the leading or the trailing edge. While compressibility effects are relatively unimportant at very low Mach numbers, frictional heat generation and thermal gradient normal to the surface could play important roles in generation and propagation of sound in high speed jets of practical interest. A general expression is given for the spectral density of the far field sound as governed by the variable density Pridmore-Brown equation. The propagation Green's function is solved numerically for a high aspect-ratio rectangular jet starting with the boundary conditions on the surface and subject to specified mean velocity and temperature profiles between the surface and the observer. It is shown the magnitude of the Green's function decreases with increasing source frequency and/or jet temperature. The phase remains constant for a rigid surface, but varies with source location when subject to an impedance type boundary condition. The Green's function in the absence of the surface, and flight effects are also investigated.

1. Introduction

COMMERCIAL aviation in the U.S. is projected to increase by 70% in the period 2010 – 2030, resulting in more exposure to air traffic noise in the communities surrounding airports. Under the Fundamental Aeronautics Program at NASA, the Fixed Wing (FW) Project is tasked with exploring concepts and technologies that could significantly improve energy efficiency and environmental compatibility of the fixed wing subsonic transport aircraft [1]. FW research focuses on vehicles that are three generations (N+3) beyond current state of the art (N) aircraft, with noise reduction goals of -52dB by 2025-30 time frame (referenced to 737-800 aircraft with CFM56-7B engines). In 2008, NASA instigated a call for conceptual design of future commercial transport in order to meet specific goals related to noise, air pollution, and fuel consumption. Early studies indicated that both propulsion system and engine placement have to be modified in order to achieve these new objectives. In particular, placement of the aircraft engine for the purpose of reduced community noise poses new challenges in structural design, material selection and computation. Configurations such as over the wing engine mount, distributed propulsion, Hybrid Wing Body (HWB) concept, and/or high aspect ratio rectangular exhaust geometry with extended beveled surfaces shield noise from reaching the ground. These concepts also produce new noise sources due to scrubbing of the flow past structure, skin vibration, boundary layer (BL) noise, and edge noise due to the scattering of sound from sharp edges.

In 2010, a series of tests were initiated at NASA Glenn Research Center in order to study the propulsion/airframe integration. These experiments, under the umbrella of "Jet-Surface Interaction Tests (JSIT)," were intended to guide analytical studies towards development of prediction model. The initial tests consisted of placement of a flat plate in the proximity of a round jet. Details of the experimental setup and test cofigurations are provided by C. Brown [2], and G. Podboy [3]. Measurements were gathered on both sides of the plate, commonly referred to as the reflected and shielded sides. In addition to the far-field microphone noise measurements [2], phased array source localization experiments [3] were also carried out in order to shed light on the noise source location and its frequency content under different exhaust conditions.

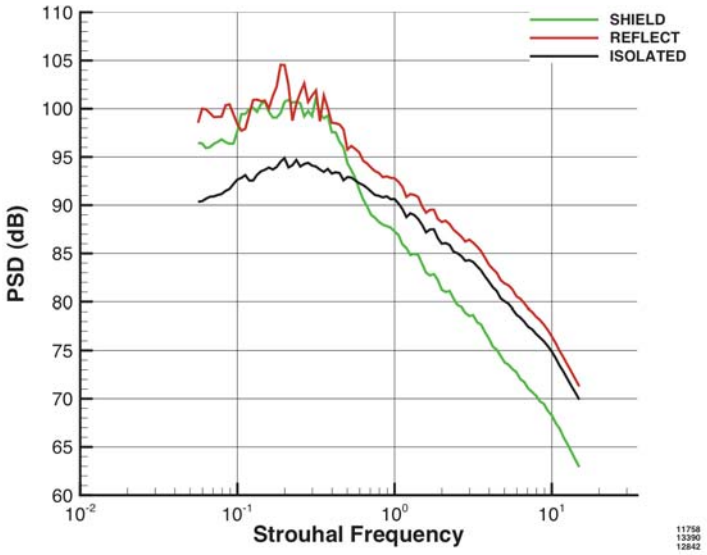

Figure 1. Sample JSIT noise measurement , C. Brown [Ref. 2].

An example of JSIT noise data that shows power spectral density per Strouhal frequency in a 2-in diameter (D =5.08cm) Mach 0.97 unheated round jet, as reported by Brown [2], is shown in figure 1. Here a solid surface extending 12-diameters from jet exit in the downstream direction was positioned at $D/2$ from the jet centerline. Far-field measurements are shown at 90^o and at 100D for a jet in isolation (no solid surface), as well as shielded and reflected sides of the jet in the presence of the surface. Examples of source localization data for the above jet are reported by Podboy [3] (not shown here). These measurements present beam-form maps of the source location for an isolated jet as well as when surfaces of varying length are placed between jet and the phased array.

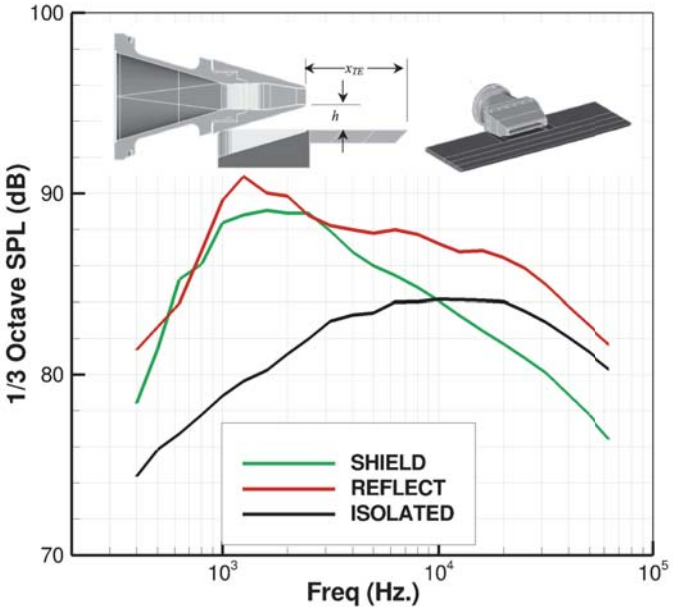

Figure 2. Jet noise spectral measurements at 90^o in a Mach 0.97 rectangular exhaust, J. Bridges [Ref. 4].

Similar measurements were reported by Bridges [4] using rectangular jets of varying aspect ratio (AR) in the proximity of a flat surface. Sample spectra are shown in figure 2 for a Mach 0.97 unheated rectangular jet (AR=8), with dimensions of (5.3566 x 0.6696-in), and the major axis parallel to the plate at standoff distance of h = 0, and plate length of X_{TE} = 12.0-in. Measurements are shown at a polar angle of 90^o, i.e., directly above or below the surface, as well as for a jet in isolation. An extensive database has been generated as a function of the jet operating conditions, length and position of the solid surface, and observer angles.

It is commonly accepted that the trailing edge noise is responsible for the enhanced low-frequency and peak noise amplitude measured on both reflected and shielded sides of the plate as seen in figures 1 and 2. A distinctive feature of the trailing edge noise component is its cardioid directivity shape and a dependence on jet velocity to the fifth power [5, 6]. Recent measurements by Lawrence *et al*. [7] indicate that the velocity power factor could be as large as 6 at longer plate length *L* that yield a wetted trailing edge. FFowcs Williams and Hall [5] describe a solution to the edge noise from a rigid plane in the presence of a turbulent flow using Lighthill's acoustic analogy. They consider a very low Mach number flow, and take advantage of an appropriate Green's function applicable to a point source in the vicinity of a half-plane [8]. Howe [9] reviews various theoretical approaches in understanding the trailing-edge noise, and summarizes diverse theories into a single model that exhibits the dependence of the acoustic field on the turbulent fluctuations near the edge as well as the significance of the Kutta condition at this point. Goldstein *et al*. [10, 11] include the effect of the mean velocity gradient on the trailing edge noise by imposing a convecting vortex source, or gust, of the general form $\Omega(x_1/U(x_3)-t, x_2, x_3)$ on a transversely sheared mean flow.

Our interest here is the turbulence-generated noise due to the scrubbing of the jet flow past an adjacent flat surface. At very low Mach number, Howe [12] describes the far-field acoustic domain in terms of the wall-pressure wave number-frequency spectrum. Various models have been suggested for wall-pressure spectrum [13] that are used in conjunction with a 2D or 3D free-space Green's function to express the far-field spectral density. These approximations ignore the mean flow refraction, compressibility effects, and sound produced outside the BL at distances that are large relative to the acoustic wavelength. At jet velocities of practical interest typical of a jet exhaust, frictional heat generation and thermal gradients in the BL could play important roles in generation and propagation of sound. Additionally, skin vibration could influence the surface boundary conditions and the subsequent radiated sound.

In sections 2 and 3 we derive an expression for the propagation Green's function (GF) applicable to the scrubbing noise on a flat surface. The GF needs to be obtained numerically when the mean flow profiles are non-uniform. An expression for the far-field pressure is given in section 4. Ideally a Reynolds-Averaged Navier-Stoke (RANS) solution for the jet in the proximity of the surface provides the mean flow and turbulence information required in evaluating both the source strength and the GF. A 2D approximation of the GF (when the flow is infinitely long in transverse x_2 direction) is discussed in section 5. Sample GF computations using analytical profiles for the mean flow and a summary are provided in sections 6 and 7.

2. Formulation of the Scrubbing Noise Problem

Consider turbulence-generated noise due to the scrubbing of a jet flow with an adjacent flat plane (Fig. 3). The governing acoustic perturbations may be obtained by writing the Navier-Stokes (NS) equations as a set of mean flow equations (referred to as a non-radiating base flow), plus a set of linear equations for the fluctuating components of the motion. By selecting a set of five appropriately defined perturbation variables, four of them non-linear, Goldstein [14] shows that the left-hand side of the acoustic equations resemble those obtained by linearizing the convective form of Euler equations about a similar base flow. Further, by assuming the mean flow as locally parallel, the factors on the left-hand side of momentum and energy equations that explicitly depend on the viscous stresses reduce to higher order terms and are neglected. These equations would then convert to inhomogeneous Rayleigh equations where the viscosity effect only appears as a non-linear source term.

In formulating the scrubbing noise problem, the mean flow is represented as a two-dimensional sheared flow. We consider the mean static pressure $\overline{p}$ within the BL to be a constant. At very low Mach numbers the compressibility effects may be negligible, however at Mach numbers typical of a jet exhaust, frictional heat generation and thermal gradients in the BL could play important roles in generation and propagation of sound. The RANS solution (which is now considered as the base flow) provides such effects via the action of viscosity near the surface. Hence by maintaining the compressibility effect, noise generation due to the scrubbing of a jet past a nearby surface is, in general, described by full acoustic analogy as considered in Appendix-A, and by Pridmore-Brown equation within a locally parallel mean flow approximation [15]

$$L\pi' = \Gamma, \qquad \pi' \simeq \frac{p'(\vec{x},t)}{\gamma \bar{p}}. \tag{1}$$

The linear operator L is

$$L \equiv D\left(D^2 - \frac{\partial}{\partial x_j}(c^2 \frac{\partial}{\partial x_j}) \right) + 2c^2 \frac{\partial U}{\partial x_j} \frac{\partial^2}{\partial x_1 \partial x_j}, \quad D \equiv \frac{\partial}{\partial t} + U \frac{\partial}{\partial x_1} . \tag{2}$$

The pressure variable π' consists of additional (higher order) terms that reduce to zero in the far field acoustic domain, and the source term $\Gamma(\vec{x},t)$ on the right hand side of (1) is defined according to the generalized acoustic analogy [14].

$$\Gamma = \frac{1}{\gamma \bar{p}} \left(-D \frac{\partial}{\partial x_i}(c^2 \frac{\partial e_{ij}}{\partial x_j}) + 2c^2 \frac{\partial U}{\partial x_j} \frac{\partial^2 e_{ij}}{\partial x_1 \partial x_i} + D^2 Q \right), \tag{3a}$$

$$Q = -(\gamma - 1)\left(\frac{1}{2} D(\rho v'^2) + \frac{\partial}{\partial x_j}(\rho v_j' h_o') + (\rho v_1' v_j') \frac{\partial U}{\partial x_j} \right), \tag{3b}$$

stress tensor e_{ij} is the difference between the fluctuating and Favre-averaged Reynolds stresses

$$e_{ij} = -(\rho v_i' v_j' - \overline{\rho v_i' v_j'}), \tag{3c}$$

and h_o' denotes the fluctuations in the moving-frame stagnation enthalpy (see the nomenclature).

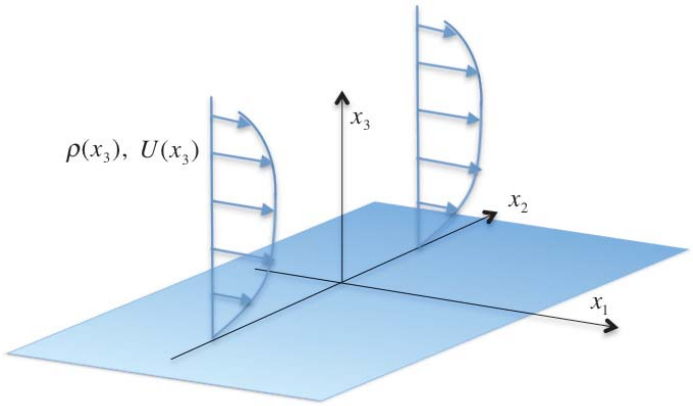

Figure 3. Jet scrubbing on a nearby surface.

The mean velocity U and density $\bar{\rho}$ are functions of the normal coordinate ($x_3 > 0$), and $c(x_3)$ is the mass-averaged speed of sound

$$U = U(x_3), \qquad c^2(x_3) = \gamma \bar{p} / \bar{\rho}(x_3). \tag{4}$$

Note that, in practice, both the mean flow and turbulence depend on the transverse direction x_2 as the source strength eventually diminishes at some distance $\pm L_2$ away from the jet centerline. In the stream-wise direction, the scrubbing effect may be limited to a distance $0 \le x_1 < L_1$, or the jet may persist beyond the plate edge at L_1 where

interaction of the turbulence with the trailing edge produces edge noise. Here, in formulating the scrubbing noise problem, we limit the source to a finite x_2 span by considering the mean flow as locally parallel in both x_1 and x_2 directions – thus expressing the problem in three dimensions. This assumption, although more suited to jets with a high aspect-ratio rectangular exhaust, permits source-volume integration within the wetted span in the x_2 direction. A round jet may be transformed into a rectangular strip by using an appropriate conformal mapping transformation. When all changes in span-wise x_2 direction are neglected, the sound intensity should be expressed as per unit thickness. The special 2D case will be discussed in section 5.

We seek a solution to equation (1) of the form

$$\pi'(\vec{x},t) = \int_{\vec{y}} \int_{\tau} G(\vec{x},t \mid \vec{y},\tau)\Gamma(\vec{y},\tau)d\tau d\vec{y} \ , \tag{5}$$

where G denotes the GF

$$LG(\vec{x},t \mid \vec{y},\tau) = \delta(\vec{x}-\vec{y})\delta(t-\tau) \ . \tag{6}$$

In a bounded medium, the above form of the solution implies that the GF satisfies certain boundary conditions on the surface. The source-volume integration in (5) is carried out over noise-generating region $\vec{y}$ in the vicinity of the scrubbing surface and at the emission time τ. The solution described here excludes the trailing edge noise that travels to the opposite side of the surface as alluded to earlier. This latter noise component requires a Wiener-Hopf type solution.

We define a Fourier Transform (FT) pair with respect to (x_1, x_2) coordinates as well as time t. The corresponding wave number vector is denoted as $\vec{k}_t = (k_1, k_2)$

$$\begin{aligned}
\hat{G}(\vec{k}_t, x_3 \mid y_3, \omega) &= \frac{1}{(2\pi)^3} \int_{-\infty}^{\infty} \int_{-\infty}^{\infty} \int_{-\infty}^{\infty} G(\vec{x},t \mid \vec{y},\tau) e^{-i[k_1(x_1-y_1)+k_2(x_2-y_2)-\omega(t-\tau)]} d(x_1-y_1)d(x_2-y_2)d(t-\tau) \ , \\
G(\vec{x},t \mid \vec{y},\tau) &= \int_{-\infty}^{\infty} \int_{-\infty}^{\infty} \int_{-\infty}^{\infty} \hat{G}(\vec{k}_t, x_3 \mid y_3, \omega) e^{i[k_1(x_1-y_1)+k_2(x_2-y_2)-\omega(t-\tau)]} dk_1 dk_2 d\omega \ .
\end{aligned} \tag{7}$$

Throughout, a circumflex is used to denote a FT variable as defined above.

The transform of equation (6) is

$$\frac{\partial^2 \hat{G}}{\partial x_3^2} + \left(\frac{(c^2)'}{c^2} - \frac{2k_1 U'}{-\omega + k_1 U} \right) \frac{\partial \hat{G}}{\partial x_3} + \left(\frac{(-\omega + k_1 U)^2}{c^2} - k_1^2 - k_2^2 \right) \hat{G} = \frac{i}{(2\pi)^3} \frac{\delta(x_3 - y_3)}{c^2(-\omega + k_1 U)} \ , \tag{8}$$

where prime notation, as used on mean variables c^2 and U, signifies differentiation with respect to normal distance x_3. The equation possesses a critical point at x_3 where factor $-\omega + k_1 U(x_3)$ vanishes. To avoid this singularity we require $k_1 < \omega / U_e$ where U_e denotes some peak mean velocity in the BL. This upper limit for k_1 is usually referred to as the non-convective domain for the wave number. As discussed in [16, 17], in the convective domain $k_1 > \omega / U_e$ it becomes necessary to provide a loss mechanism, such as turbulent viscosity, in order to avoid the singularity. The dominant value of k_1 contributing to the far-field noise will be determined in section 3. It will be shown that when $U_e < c_\infty$ the upper limit condition stated for k_1 will be satisfied at all observer location.

For convenience, the second-order linear differential equation (8) is rearranged as

$$\frac{\partial^2 \breve{G}}{\partial x_3^2} + f(\vec{k}_t, x_3, \omega)\breve{G} = \delta(x_3 - y_3) \ . \tag{9}$$

Since equation (9) is self-adjoint, the newly defined GF, $\breve{G}$, is symmetric in (x_3, y_3)

$$\breve{G}(\vec{k}_t, x_3 \mid y_3, \omega) = \breve{G}(\vec{k}_t, y_3 \mid x_3, \omega) \ ,$$

and is related to the GF of interest $\hat{G}$ as

$$\hat{G}(\vec{k}_t, x_3 \mid y_3, \omega) = \frac{i}{(2\pi)^3} \frac{1}{c(y_3)c(x_3)} \frac{-\omega + k_1 U(x_3)}{\left(-\omega + k_1 U(y_3)\right)^2} \breve{G}(\vec{k}_t, x_3 \mid y_3, \omega) \ , \tag{10}$$

where

$$f(\vec{k}_t, x_3, \omega) = \chi^2 - \mathbb{C}^2 - \frac{2(k_1 U')^2}{(-\omega + k_1 U)^2} + \frac{k_1 U''}{-\omega + k_1 U} + \frac{(c^2)'}{c^2} \frac{k_1 U'}{-\omega + k_1 U} \ ,$$

$$\chi^2(\vec{k}_t, x_3, \omega) = \frac{(-\omega + k_1 U)^2}{c^2} - k_1^2 - k_2^2 \ , \tag{11}$$

$$\mathbb{C}^2(x_3) = \frac{1}{2} \frac{\partial}{\partial x_3} \left(\frac{(c^2)'}{c^2} \right) + \frac{1}{4} \left(\frac{(c^2)'}{c^2} \right)^2 \ ,$$

and $(c^2)' / c^2 = (\partial \overline{\rho} / \partial x_3) / \overline{\rho}$.

It should be noted that unlike the present problem, the full propagation equations (i.e. not locally parallel) might not reduce to a self-adjoint form. Such is the case when the governing equations are written for a spreading flow [18]. In that case, working with the adjoint GF will entail additional integrals that should be carried out on the surfaces. A general solution for the five field variables using a vector GF formulation is provided in Appendix A. The second integral in equation (A16) in the appendix describes the contribution to the acoustic field due to the nearby surfaces. In the formulation described herein, the GF satisfies conditions that make the surface integral equal to zero.

Far away from the noise generating region, as $x_3 \to \infty$ the mean velocity and the sound speed approach their respective ambient values U_∞ and c_∞, and equations (9) and (11) show that

$$\frac{\partial^2 \breve{G}}{\partial x_3^2} + \chi_\infty^2 \breve{G} = 0, \quad x_3 \to \infty \tag{12a}$$

where

$$\chi_\infty^2 = (-\kappa_o + k_1 M_\infty)^2 - k_1^2 - k_2^2 \ ; \quad \kappa_o = \omega / c_\infty \ , \quad M_\infty = U_\infty / c_\infty \ . \tag{12b}$$

The Mach number M_∞ takes account of the flight effect when surface is in motion relative to the ambient. The far-field solution to equation (12a) is

$$\breve{G}(\vec{k}_t, x_3 \mid y_3, \omega) = b \ e^{-i\chi_\infty x_3}, \quad x_3 \to \infty \tag{13}$$

where complex number *b* has dimension of length, and depends on $\vec{k}_t$ and ω . An outgoing propagating wave ($x_3 > 0$) requires the negative root of χ_∞^2 when $\chi_\infty^2 > 0$. When $\chi_\infty^2 < 0$ the pressure decays exponentially normal to the surface (evanescent waves), and the branch-cut is chosen such that $\chi_\infty = -i(|\chi_\infty^2|)^{1/2}$. Aerodynamic

noise scattered off the edge of a half-plane is sometimes described as the interaction of evanescent waves (rather than propagating acoustic waves) with the edge [19, 20]. These disturbances are dominated by spectral components that possess a subsonic phase velocity in a constant x_3 plane.

Since we are interested in the scrubbing noise that reaches a distant observer, the radiation field would be dominated by wave numbers, in constant x_3 plane, that possess a supersonic phase velocity

$$\frac{\omega}{M_\infty k_1 + \sqrt{k_1^2 + k_2^2}} > c_\infty \ . \tag{14}$$

A no slip boundary condition on the mean flow $(U = 0, x_3 \to 0)$ combined with the x_3 component of the linearized momentum equation within the turbulent boundary layer (TBL) shows that

$$\frac{\partial(\rho v_3')}{\partial t} + \frac{\partial p'}{\partial x_3} = 0, \qquad x_3 = 0 \tag{15}$$

Upon replacing ρ with the mean fluid density ρ_o near the surface, we apply a FT to the latter equation to obtain

$$-i\omega\rho_o \widehat{v_3'} + \frac{\partial \widehat{p'}}{\partial x_3} = 0, \qquad x_3 = 0 \tag{16}$$

Assuming that Fourier components of the normal velocity and pressure on the surface relate through the surface impedance $Z(\omega)$ as

$$\widehat{p'} = Z\,\widehat{v_3'}\,, \qquad x_3 = 0 \tag{17}$$

we find

$$\frac{\partial \widehat{\pi'}}{\partial x_3} - \frac{i\rho_o\omega}{Z}\widehat{\pi'} = 0, \qquad x_3 = 0 \ . \tag{18}$$

Since the FT of a convolution is the product of the Fourier transforms, equation (5) implies

$$\widehat{\pi'}(\vec{k}_t, x_3, \omega) = (2\pi)^3 \int_{y_3} \hat{G}(\vec{k}_t, x_3 \mid y_3, \omega)\hat{\Gamma}(\vec{k}_t, y_3, \omega)\, dy_3 \ , \tag{19}$$

and upon using (19) in (18) we find

$$\frac{\partial \hat{G}}{\partial x_3} - \frac{i\rho_o\omega}{Z}\hat{G} = 0, \qquad x_3 = 0 \ . \tag{20}$$

Our interest is in the boundary condition applicable to $\breve{G}$ rather than $\hat{G}$. Substituting equation (10) in (20) shows that

$$\frac{\partial \breve{G}}{\partial x_3} - \psi\breve{G} = 0\,, \qquad x_3 = 0 \ , \tag{21a}$$

$$\psi(k_1,\omega,\overline{Z})=\left(\frac{i\kappa_o}{\overline{Z}}\frac{c_\infty^2}{c_o^2}+\frac{c_o'}{c_o}+\frac{k_1}{\omega}U'(0)\right),\quad \overline{Z}(\omega)\equiv\frac{Z(\omega)}{\rho_\infty c_\infty} \tag{21b}$$

where c_o is the mean sound speed in the fluid at the surface interface, and c_o' is its derivative at x_3 = 0. An alternative way of deriving the surface boundary condition (21a) is described in Appendix B.

The problem at hand is thus reduced to solving equation (9) subject to the two boundary conditions (14) and (21).

The GF in equation (9) may be expressed in terms of two linearly independent solutions $V_j(\vec{k}_t,x_3,\omega)$ to the homogeneous equation

$$\partial^2 V_j/\partial x_3^2+fV_j=0,\qquad j=1,2 \tag{22}$$

such that V_1 and V_2 satisfy the homogeneous boundary conditions at 0 and ∞, respectively. For brevity we omit $\vec{k}_t$ and ω from the arguments of V_1 and V_2.

$$\frac{\partial V_1(x_3)}{\partial x_3}-\psi V_1(x_3)=0,\quad x_3=0 \tag{23a}$$

$$\frac{\partial V_2(x_3)}{\partial x_3}+i\chi_\infty V_2=0,\quad x_3\to\infty \tag{23b}$$

and

$$\breve{G}(\vec{k}_t,x_3\,|\,y_3,\omega)=\begin{vmatrix} V_2(x_3)V_1(y_3)/W(y_3), & y_3<x_3\\ V_1(x_3)V_2(y_3)/W(y_3), & y_3>x_3\end{vmatrix} \tag{24}$$

and $W\left(V_1(y_3),V_2(y_3)\right)=V_1V_2'-V_1'V_2$ is the Wronskian. For convenience both V_1 and V_2 are normalized at zero argument $y_3=0$ such that

$$V_1(0)=V_2(0)=1, \tag{25}$$

and since according to Abel's formula the Wronskian to equation (22) is independent of y_3, then we evaluate $W=W_o$ at the surface. Equations (23a) and (25) conclude that

$$W_o(\vec{k}_t,\omega,\overline{Z})=V_2'(0)-\psi(k_1,\omega,\overline{Z}). \tag{26}$$

The above expression shows that the Wronskian W_o depends on the BL velocity and temperature profiles at $y_3=0$, as well as the surface impedance $\overline{Z}$ through parameter ψ. It is noted that equation (22) supports Helmholtz instabilities that would arise when $\vec{k}_t$ and ω satisfy the Eigen-wave condition $W_o(\vec{k}_t,\omega,\overline{Z})=0$. The instability waves could be triggered when the BL profile supports the Eigen-wave condition. These waves could grow exponentially and dominate the region they occupy. Consequently, we need to set the wave number limit to avoid these special cases. Jones [21] studied the instability of a two-dimensional shear layer using a model velocity profile in which the velocity increased linearly from 0 to U_e over a distance of h from the surface and then remained constant. He showed that the onset of Helmholtz instabilities occur at a Strouhal frequency of $\omega h/U_e\sim 1/3$

where ω denotes the frequency of sound waves falling on the shear layer. At frequencies above this critical value the layer remained stable.

Upon placing (24) into (10), the Fourier transformed GF at an observer point above the source region is given as

$$\hat{G}(\vec{k}_t, x_3 \mid y_3, \omega) = \frac{i}{(2\pi)^3} \frac{1}{c(y_3)c(x_3)} \frac{-\omega + k_1 U(x_3)}{\left(-\omega + k_1 U(y_3)\right)^2} \frac{V_2(x_3) V_1(y_3)}{W_o}, \quad x_3 > y_3 \tag{27}$$

An alternative form of the GF valid for $x_3 < y_3$ (see equation 24) should be used if one were interested in the surface pressure. The two functions V_i are determined numerically. The first variable is evaluated when equation (22) is solved as an initial value problem with $V_1(0) = 1$ and $V_1'(0) = \psi$. The second variable is determined when (22) is solved as a boundary value problem subject to $V_2(0) = 1$, and $V_2'(x_3) + i\chi V_2(x_3) = 0$ as $x_3 \to \infty$. Fortunately, as we shall see next, there are only certain values of wave numbers k_1 and k_2 that make the major contribution to the radiated far-field noise.

3. Stationary Phase Solution

We apply an inverse FT with respect to wave numbers k_1 and k_2 and write the GF as

$$\mathbf{G}(\vec{x}, \vec{y}; \omega) = \int_{-\infty}^{\infty} \int_{-\infty}^{\infty} \hat{G}(\vec{k}_t, x_3 \mid y_3, \omega) e^{i[k_1(x_1 - y_1) + k_2(x_2 - y_2)]} dk_1 dk_2 \ . \tag{28}$$

Since the interest is in the far-field noise, the appropriate form for V_2 is

$$V_2(\vec{k}_t, x_3, \omega) = b_2 e^{-i\chi_\infty x_3}, \qquad x_3 \to \infty \ . \tag{29}$$

Complex number $b_2(\vec{k}_t, \omega)$ has a dimension of unity, and should be a known parameter once the boundary value problem (22) is solved for V_2. Placing (27) and (29) into (28), the double integral involving wave numbers k_1 and k_2 becomes

$$\mathbf{G}(\vec{x}, \vec{y}; \omega) = \frac{i}{(2\pi)^3} \frac{1}{c(y_3)c(x_3)} \int_{k_1} \int_{k_2} \frac{-\omega + k_1 U(x_3)}{\left(-\omega + k_1 U(y_3)\right)^2} \frac{b_2 V_1(\vec{k}_t, y_3, \omega)}{W_o(\vec{k}_t, \omega, \bar{Z})} e^{i\Theta(\vec{k}_t, \vec{x}, \omega)} dk_1 dk_2 \ , \tag{30}$$

where

$$\Theta(\vec{k}_t, \vec{x}, \omega) = k_1(x_1 - y_1) + k_2(x_2 - y_2) - \chi_\infty x_3 \ , \tag{31}$$

and χ_∞ was defined in equation (12b). We adopt a spherical coordinate system where θ is the angle the observer position vector makes with the direction of the mean flow (Fig. 4)

$$(x_1 - y_1, x_2 - y_2, x_3) = R(\sin\phi\cos\theta,\ \cos\phi,\ \sin\phi\sin\theta), \tag{32}$$

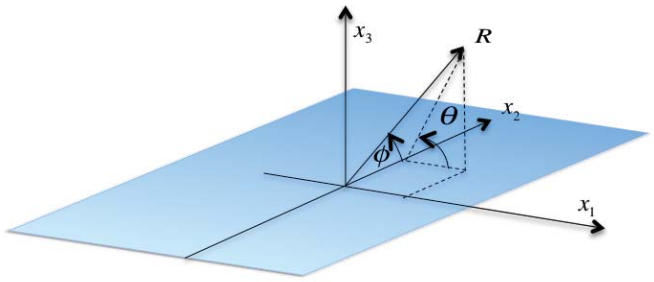

Figure 4. Spherical coordinates $0 \le \theta \le \pi,\ 0 \le \phi \le \pi$.

where $R = |\vec{x} - \vec{y}|$. The wave number vector in expressed in a similar fashion as

$$(k_1, k_2, k_3) = \kappa_o(\sin\phi'\cos\theta',\ \cos\phi',\ \sin\phi'\sin\theta')\ . \tag{33}$$

Using (32) and (33) in (31), the phase factor becomes

$$\Theta(\vec{k}_t, \vec{x}, \omega) = R\kappa_o\left(\sin\phi\cos\theta\sin\phi'\cos\theta' + \cos\phi\cos\phi' - \sin\phi\sin\theta\ S(\theta', \phi', M_\infty)\right), \tag{34}$$

where real function S is taken as the negative root of S^2 for those values of (θ', ϕ') that lend to a positive S^2

$$S^2(\theta', \phi', M_\infty) = \left(1 - (1 - M_\infty^2)\cos^2\theta'\right)\sin^2\phi' - 2M_\infty\cos\theta'\sin\phi'\ . \tag{35}$$

Note that far-field radiation condition (14) combined with (33) also leads to the requirement that $S^2 > 0$.

The large parameter in applying the stationary phase technique [22] is $R\kappa_o \gg 1$. This requires the source to observer distance *R* to be much larger than the wavelength of the radiated sound. If we define a Strouhal frequency as $St = \omega\delta_o / U_e$, where δ_o is the BL thickness (distance from the wall at which the mean velocity is $0.99U_e$), then the large parameter requirement implies $St >> c_\infty\delta_o / (U_e R)$ which is not a very stringent condition even at relatively low frequency.

The Jacobian in making coordinates transformation from (k_1, k_2) to (θ', ϕ') is $\kappa_o^2\sin\theta'\sin^2\phi'$ or $dk_1 dk_2 = \kappa_o^2\sin\theta'\sin^2\phi' d\theta' d\phi'$.

Using the new coordinates, the point of stationary phase, denoted as (θ^s, ϕ^s), is obtained when we set equal to zero the two partial derivatives of phase factor Θ

$$\frac{\partial\Theta}{\partial\theta'} = 0, \quad \frac{\partial\Theta}{\partial\phi'} = 0\ . \tag{36}$$

It can be shown that the stationary-point angles are related to observer angles (θ, ϕ) as

$$\tan\theta = -S(\theta^s, \phi^s, M_\infty) / \left(M_\infty + (1 - M_\infty^2)\cos\theta^s\sin\phi^s\right)\ , \tag{37}$$

$$\sin\theta\tan\phi = -S(\theta^s, \phi^s, M_\infty) / \cos\phi^s\ . \tag{38}$$

In the absence of flight effect we find

$$\theta^s = \theta, \quad \phi^s = \phi, \qquad (M_\infty = 0). \tag{39}$$

Equation (39) simply implies that when flight effect is small, the major contribution to the radiated sound field is due to wave numbers with magnitude κ_o in the same direction as the observer point (θ,ϕ). When $\phi \neq \pi/2$ the two equations (37) and (38) need to be solved numerically using Newton-Raphson iteration method to determine the stationary point angles as a function of the observer angles and flight Mach number. In the special case when $\phi = \pi/2$ equation (38) shows that $\phi^s = \pi/2$, and from (37) we find

$$\cos\theta^s = \frac{1}{1-M_\infty^2}\left(-M_\infty + \frac{\cos\theta}{\sqrt{1-M_\infty^2\sin^2\theta}}\right), \quad \phi = \frac{\pi}{2} \quad . \tag{40}$$

Figure 5 shows the range of polar angle θ that are subject to acoustic radiation from the surface at flight when $\phi = \pi/2$. It is seen that the minimum value of θ^s as well as the maximum value of θ are affected by flight. When $\phi \neq \pi/2$ the stationary-point angles vary with both observer angles. A sample example is illustrated in Fig. 6 at a selective value of $\phi = \pi/4$.

The contribution to the integral in equation (30) in the vicinity of the stationary point is obtained when we expand phase factor Θ (to second order) about this point and evaluate the rest of the integrand at the point of stationary phase $\vec{k}_t^{\,s} = (k_1^s, k_2^s)$.

$$\vec{k}_t^{\,s} = \kappa_o(\sin\phi^s\cos\theta^s,\ \cos\phi^s), \tag{41}$$

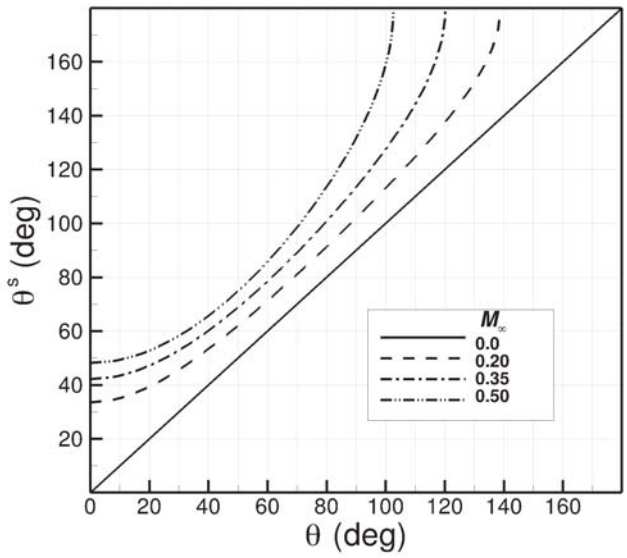

Figure 5. Stationary point angles in flight ($\phi = \phi^s = \pi/2$).

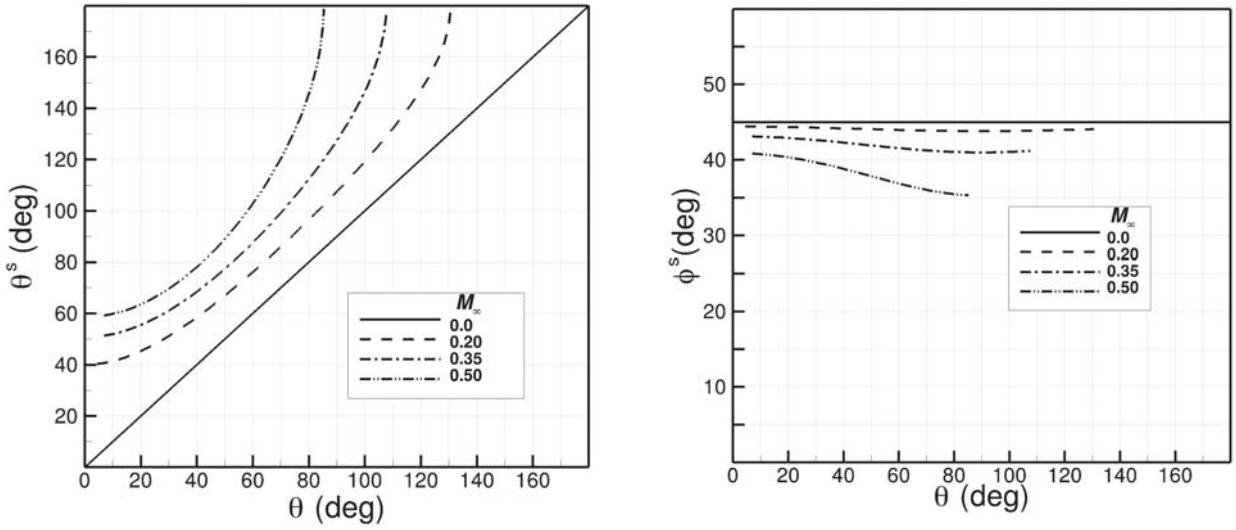

Figure 6. Stationary point angles θ^s and ϕ^s in flight at $\phi = \pi/4$.

$$\mathbf{G}(\vec{x},\vec{y};\omega) \sim -i\frac{e^{i\Theta(\vec{k}_t^s,\vec{x},\omega)}}{(2\pi)^3 R}\frac{\sin\theta^s \sin^2\phi^s}{c_\infty^2 c(y_3)}\frac{b_2(\vec{k}_t^s,\omega)V_1(\vec{k}_t^s,y_3,\omega)}{W_o\left(\vec{k}_t^s,\omega,\bar{Z}\right)}\frac{(1-M_\infty \sin\phi^s\cos\theta^s)\,\Im}{\left(1-\dfrac{U(y_3)}{c_\infty}\sin\phi^s\cos\theta^s\right)^2}, \tag{42}$$

as $R \to \infty$, and

$$\Im = \int_{-\infty}^{\infty}\int_{-\infty}^{\infty} \exp\left(-\frac{i}{2}(A_1\alpha^2 + A_2\beta^2 + 2A_3\alpha\beta)\right) d\alpha d\beta \ . \tag{43}$$

Parameters $A_i\,(i=1,2,3)$ are coefficients in the second-order expansion of the phase factor about the stationary point

$$A_1 = -\frac{1}{R\kappa_o}\frac{\partial^2\Theta(\vec{k}_t^s,\vec{x},\omega)}{\partial\theta^{s\,2}}, \qquad A_2 = -\frac{1}{R\kappa_o}\frac{\partial^2\Theta}{\partial\phi^{s\,2}}, \qquad A_3 = -\frac{1}{R\kappa_o}\frac{\partial^2\Theta}{\partial\theta^s\ \partial\phi^s}, \tag{44}$$

and $\Theta(\vec{k}_t^s,\vec{x},\omega)$ is evaluated from (34) and (35) subject to the condition stated earlier for *S*. General expressions for coefficients A_i are provided in Appendix C. It is seen that the coupling term A_3 vanishes when $\phi = \pi/2$. The double integral in (43) is evaluated in closed form as

$$\Im = \frac{2\pi}{\sqrt{|\,A_1A_2 - A_3^2\,|}}\exp\left(-\frac{\pi i}{4}\mathrm{sgn}(A_1 - \frac{A_3^2}{A_2}) - \frac{\pi i}{4}\mathrm{sgn}(A_2)\right) \ . \tag{45}$$

In the absence of flight it is readily shown that $\Im = -2\pi i/\sin\phi$, and $\Theta = \kappa_o R$. Subsequently

$$\mathbf{G}(\vec{x},\vec{y};\omega)\sim -\frac{e^{i\kappa_o R}}{(2\pi)^2 R}\frac{\sin\theta\sin\phi}{c_\infty^2 c(y_3)}\frac{b_2(\vec{k}_t^{\,s},\omega)V_1(\vec{k}_t^{\,s},y_3,\omega)}{W_o\left(\vec{k}_t^{\,s},\omega,\bar{Z}\right)}\frac{1}{\left(1-\frac{U(y_3)}{c_\infty}\sin\phi\cos\theta\right)^2},\quad (M_\infty=0) \qquad (46)$$

where $\vec{k}_t^{\,s}=\kappa_o(\sin\phi\cos\theta,\ \cos\phi)$. Note that when $k_1=\kappa_o\sin\phi\cos\theta$, the upper limit placed on k_1 in section 2 will be satisfied at all subsonic conditions $U_j/c_\infty<1$. At supersonic conditions only certain observer locations will be subject to the critical layer singularity.

The GF $G(\vec{x},t\mid\vec{y},\tau)$ is now obtained as

$$G(\vec{x},t\mid\vec{y},\tau)=\int_{-\infty}^{\infty}\mathbf{G}(\vec{x},\vec{y};\omega)e^{-i\omega(t-\tau)}d\omega\,. \qquad (47)$$

Appendix D shows that equation (42) is also applicable to the acoustics of an unbounded medium (in the absence of a scrubbing surface) provided that the two linearly independent solutions V_1 and V_2 to equation (22) are evaluated subject to appropriate boundary conditions at $x_3\to\pm\infty$.

4. Far-field Acoustics

The spectral density of the far-field sound is a FT of the pressure auto-covariance

$$\overline{p^2}(\vec{x},\omega)=(\gamma\bar{p})^2\int_{-\infty}^{\infty}e^{i\omega\tau}\left[\frac{1}{2T}\int_{-T}^{T}\pi'(\vec{x},t)\pi'(\vec{x},t+\tau)dt\right]d\tau\ . \qquad (48)$$

where *T* denotes some large time. Upon placing (5) and (47) into (48), it is shown that [23]

$$\overline{p^2}(\vec{x},\omega)=\int_{\vec{y}}\int_{\vec{\xi}}\int_{\tau=-\infty}^{\infty}\mathbf{G}^*(\vec{x},\vec{y}-\vec{\xi}/2;\omega)\mathbf{G}(\vec{x},\vec{y}+\vec{\xi}/2;\omega)q(\vec{y},\vec{\xi},\tau)e^{i\omega\tau}d\tau d\vec{\xi}d\vec{y}\ , \qquad (49)$$

where *q* denotes a two-point space-time correlation between noise generating sources at points A and B separated by space $\vec{\xi}$ and time τ, and superscript * denotes a complex conjugate. Using the source term in equation (1) we have

$$q(\vec{y},\vec{\xi},\tau)=(\gamma\bar{p})^2\frac{1}{2T}\int_{-T}^{T}\Gamma(\vec{y}-\vec{\xi}/2,t)\Gamma(\vec{y}+\vec{\xi}/2,t+\tau)dt,\quad T\to\infty\ . \qquad (50)$$

Since the exponential phase factor in the GF equation (46) depends on the distance $R=|\vec{x}-\vec{y}|$ between observer point $\vec{x}$ and source point $\vec{y}$, the product of the GF and its conjugate is evaluated at the center of the correlation multiplied by a phase factor $\exp(-i\vec{k}.\vec{\xi})$, where wave number $\vec{k}$ is directed as $\vec{x}-\vec{y}$ and has a magnitude of κ_o

$$\overline{p^2}(\vec{x},\omega)=\int_{\vec{y}}|\mathbf{G}(\vec{x},\vec{y};\omega)|^2\int_{\vec{\xi}}\int_{\tau=-\infty}^{\infty}q(\vec{y},\vec{\xi},\tau)e^{i\omega\tau-i\vec{k}.\vec{\xi}}d\tau d\vec{\xi}d\vec{y}\ . \qquad (51)$$

As is a common practice in acoustic analogy noise-prediction models, the space-time FT of the source correlation function, denoted as the inner double integral in (51), is evaluated in closed-form once an acceptable physics-based source model is obtained. The modeling becomes much less cumbersome if the spatial derivatives present in the source were to be transferred to the GF within equation (5) and prior to forming the sound spectral density function. Consequently, the GF could be subject to new spatial derivatives at the source point $\vec{y}$ while source $\Gamma(\vec{y},t)$ would be free of similar derivatives.

Since the GF depends on both V_1 and V_2, which in turn depend on ω, θ, and ϕ, the pair (V_1,V_2) is determined numerically per pre-selected observer angles and frequency using the local BL mean velocity and density profiles. The integral over the source region in equation (49) is then evaluated to obtain the far-field noise as a contribution from independent correlation volume elements that comprise the source. As pointed out earlier, the volume integration is limited to regions with relatively stronger source strength while the mean flow is considered as locally parallel in both x_1 and x_2 directions.

In the limit of very low Mach number ($M < 0.10$), it is argued [12] that there is a direct correspondence between the acoustic domain of the wall-pressure spectrum and the far-field spectral density of the radiated sound. This approximation ignores mean flow refraction and sound produced by the turbulence outside the boundary layer at distances that are not small relative to the acoustic wavelength. Following this argument, at large distance *R* from a hard wall region of area *A*, Howe [24] proposed an expression for the sound spectral density in terms of the so-called blocked pressure, which in the present notation is

$$\overline{p^2}(\vec{x},\omega) = A\kappa_o^2 \frac{\sin^2\theta \sin^2\phi}{R^2} P(\vec{k}_t,\omega) \ , \tag{52}$$

where $P(\vec{k}_t,\omega)$ is the wall-pressure wave number-frequency spectrum, and is defined as a FT of the space-time pressure correlation function $q(\xi_1,\xi_2,\tau)$ of the wall-pressure

$$P(\vec{k}_t,\omega) = \frac{1}{(2\pi)^3} \int_{\tau=-\infty}^{\infty} \int_A q(\xi_1,\xi_2,\tau) \exp\left(i\omega\tau - i\vec{k}_t.\vec{\xi}_t\right) d\tau d\xi_1 d\xi_2 \ . \tag{53}$$

Here $\vec{\xi}_t$ is the spatial separation vector of the correlation on the surface and $\vec{k}_t$ is the corresponding wave-number vector. The wall-pressure correlation function over a rectangular area *A* is defined as

$$q(\xi_1,\xi_2,\tau) = \lim_{T\to\infty} \frac{1}{2T} \frac{1}{A} \int_{-T}^{T} \int_{-L_1}^{L_1} \int_{-L_2}^{L_2} p'(y_1,y_2,0,t) p'(y_1+\xi_1,y_2+\xi_2,0,t+\tau) dy_1 dy_2 dt \ . \tag{54}$$

Various models for $P(\vec{k}_t,\omega)$ have been proposed in the literature, however there is no universally accepted form for the wall-pressure spectrum that could directly be substituted into (52). For example low wave number measurements of Sevik [13] suggest

$$\frac{P(\vec{k}_t,\omega)}{\rho_\infty^2 v_*^3 \delta_o^3} \approx \frac{127(U_e/c_\infty)^2 (v_*/U_e)}{(\omega\delta_o/U_e)^{4.5}}, \quad 24 < \frac{\omega\delta_o}{U_e} < 240, \quad 0.01 < \frac{U_e}{c_\infty} < 0.15. \tag{55}$$

where $v_* \approx 0.03U_e$ is the friction velocity, and δ_o denotes the BL thickness as defined earlier.

More complicated expressions have been suggested for the wall-pressure wave number-frequency spectrum $P(\vec{k}_t,\omega)$ with additional parameters that are meant to account for the attenuation and refraction of sound in the BL [25] and/or surface roughness [26] and dependence on the individual wave number components on the surface. The

validity of these empirical models remains to be confirmed experimentally. A comparison of semi-empirical equation (52) with the analytical solution given in equation (51) shows that the latter should account for all of the above-mentioned effects when source information as well as the GF are available within and outside the BL. Ideally, a RANS solution to the wall-bounded flow would provide both the mean flow and turbulence information, such as turbulent kinetic energy and its dissipation rate, required in evaluating the GF and modeling the source autocovariance $q(\vec{y},\vec{\xi},\tau)$ in Eq. (51) within the boundary layer as well as the main jet.

5. Two-Dimensional Approximation

When the two-dimensional flow is infinitely long in transverse direction x_2 (unlike in section 3 where the rectangular flow was limited to a finite x_2 domain), the analysis is carried out in two dimensions. Following the steps outlined earlier, the new GF is obtained from an equation similar to (30)

$$\mathbf{G}(\vec{x},\vec{y};\omega)=\frac{i}{(2\pi)^2}\frac{1}{c(y_3)c(x_3)}\int_{k_1}\frac{-\omega+k_1U(x_3)}{\left(-\omega+k_1U(y_3)\right)^2}\frac{b_2V_1(k_1,y_3,\omega)}{W_o(k_1,\omega,\bar{Z})}e^{i\Theta(k_1,\vec{x},\omega)}dk_1\ , \tag{56}$$

where phase parameter is now defined as

$$\Theta(k_1,\vec{x},\omega)=k_1(x_1-y_1)-\chi_\infty x_3\ ,\quad \chi_\infty^2=(-\kappa_o+k_1M_\infty)^2-k_1^2\ . \tag{57}$$

It is readily shown that the point of stationary phase is $k_1^s=\kappa_o\cos\theta^s$, where stationary angle θ^s is solved from Eq. (40) as seen in figure 5. The GF is then written as

$$\mathbf{G}(\vec{x},\vec{y};\omega)\sim -i\frac{e^{i\Theta(k_1^s,\vec{x},\omega)}}{(2\pi)^2\sqrt{\kappa_oR}}\frac{\sin\theta^s}{c_\infty^2c(y_3)}\frac{b_2(k_1^s,\omega)V_1(k_1^s,y_3,\omega)}{W_o\left(k_1^s,\omega,\bar{Z}\right)}\frac{(1-M_\infty\cos\theta^s)\,\Im_1}{(1-\dfrac{U(y_3)}{c_\infty}\cos\theta^s)^2}, \tag{58a}$$

where

$$\Im_1=\int_{-\infty}^{\infty}\exp\left(-\frac{i}{2}A_1\alpha^2\right)d\alpha=\sqrt{\frac{2\pi}{A_1}}e^{-i\pi/4}\ . \tag{58b}$$

Coefficient A_1 is evaluated as before (see Appendix C), but with $\phi=\phi^s=\pi/2$. In the special case when $M_\infty=0$ it is seen that $A_1=1$, $\Theta(k_1^s,x,\omega)=\kappa_oR$, and $k_1^s=\kappa_o\cos\theta$. Accordingly

$$\mathbf{G}(\vec{x},\vec{y};\omega)\sim -\frac{e^{i\pi/4}}{(2\pi)^{3/2}}\frac{e^{i\kappa_oR}}{\sqrt{\kappa_oR}}\frac{\sin\theta}{c_\infty^2c(y_3)}\frac{b_2(k_1^s,\omega)V_1(k_1^s,y_3,\omega)}{W_o\left(k_1^s,\omega,\bar{Z}\right)}\frac{1}{(1-\dfrac{U(y_3)}{c_\infty}\cos\theta)^2},\quad (M_\infty=0)\ . \tag{59}$$

The source correlation now uses $\vec{\xi}=(\xi_1,\xi_3)$ as a separation vector, and the far-field sound is evaluated using equation (49) with the volume element as $d\vec{y}=dy_1dy_3$, and per unit flow thickness in x_2 direction. Note that both 3D and 2D expressions for the GF could be written in a similar from if equations (46) and (59) were normalized with respect to their corresponding free-space GF.

6. Numerical Results

Sample Green's function calculations are presented using analytical representations of the jet mean velocity and temperature profiles in the proximity of a flat surface.

The mean velocity profile adopted here depends on the normal direction y_3 only, and is modeled for a jet with thickness $D_j = 2.0$ inches

$$\frac{U(\eta)}{U_j} = \begin{cases} \tanh(\frac{D_j \eta}{d_1}), & \eta < 1.05 \\ \frac{1}{2}(1+\frac{U_\infty}{U_j}) + \frac{1}{2}(1-\frac{U_\infty}{U_j}) \tanh \frac{1}{d_2}\left(\frac{1/2}{\eta - 1} - \frac{\eta - 1}{1/2} \right), & \eta \geq 1.05 \end{cases} \tag{60}$$

where $\eta = y_3 / D_j$ is the non-dimensional distance from the wall. At $\eta \geq 1.05$ the above mean velocity decay is compatible with the well-known similarity rules of Tennekes and Lumley in the parallel flow approximation [27]. Using parameters $(d_1, d_2) = (0.10, 2.0)$, and in the absence of flight, the velocity profile divided by jet velocity U_j is plotted (Fig. 7). The boundary layer thickness for this flow is $\delta_o / D_j = 1.324 d_1$. It is noted that at the connection point $(\eta = 1.05)$, the left-hand derivative $U'(\eta)$ is zero, but the right-hand derivative is slightly different from zero, accordingly an interpolation of second-order or higher may be required in the vicinity unless this point is bypassed in the integration.

The mean static temperature is modeled as a composite of the two profiles – the first profile $T_1(\eta)$ is obtained by placing the above velocity profile in Crocco-Busemann law

$$\frac{T_1(\eta)}{T_\infty} = 1 + (T_R - 1)\frac{U(\eta)}{U_j} - \frac{\gamma - 1}{2}\left(\frac{U(\eta)}{c_\infty} \right)^2, \tag{61a}$$

where T_R is the jet plenum stagnation temperature ratio. The second profile is intended to simulate frictional heat generation in the proximity of the wall

$$\frac{T_2(\eta)}{T_\infty} = \frac{1}{d_3}\left(\frac{1}{2} + \frac{1}{2}\tanh \frac{1}{d_4}(\frac{1}{D_j \eta} - D_j \eta) \right). \tag{61b}$$

Using parameters $(d_3, d_4) = (4.0, 3.0)$ the temperature profile $T(\eta) = T_1(\eta) + T_2(\eta)$ and the sound speed $c = \sqrt{\gamma \Re T}$ are shown in Fig. 7 subject to jet exit values of $U_j / c_\infty = 0.90$, and $T_R = 3.0$.

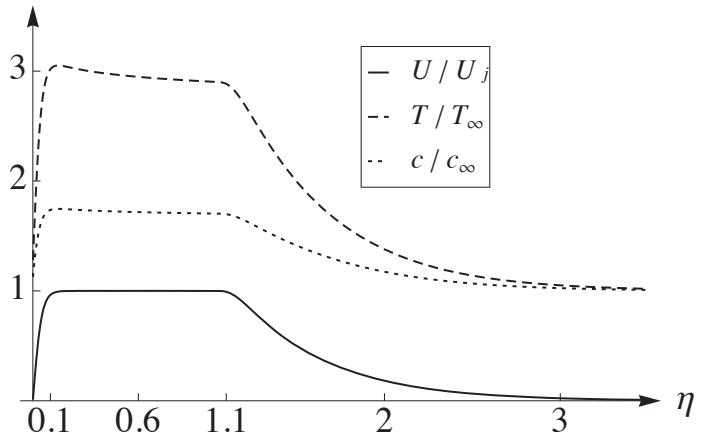

Figure 7. Profiles for mean axial velocity (solid line), static temperature (dashed line) and sound speed (dotted line) at $U_j/c_\infty = 0.90, T_R = 3.0$ **.**

The GF is solved numerically at specific values of the Strouhal frequency St_o defined as

$$St_o \equiv \frac{1}{2\pi}\frac{\omega D_j}{U_j} \ , \tag{62}$$

We define non-dimensional parameters $\bar{\kappa} = \kappa_o D_j = 2\pi\, St_o (U_j / c_\infty)$, $\bar{c} = c/c_\infty$, $\bar{U} = U/c_\infty$, $\bar{R} = R/D_j$, and divide the 3D and 2D expressions in (46) and (59) by their respective free-space values of $(-e^{i\bar{\kappa}\bar{R}}/4\pi\bar{R})$ and $(-e^{i\bar{\kappa}\bar{R}+i\pi/4}/\sqrt{8\pi\bar{\kappa}\bar{R}}\,)$. Additionally constant $1/(\pi c_\infty^3)$ is factored out in order to define a normalized GF applicable to the far field. In the absence of flight effect we have

$$G_N(\eta,\omega) = \left| \begin{array}{ll} \dfrac{\sin\theta\sin\phi}{\bar{c}}\dfrac{b_2(\vec{k}_t^{\,s},\omega)V_1(\vec{k}_t^{\,s},\eta,\omega)}{\bar{W}_o(\vec{k}_t^{\,s},\omega,\bar{Z})}\dfrac{1}{(1-\bar{U}\sin\phi\cos\theta)^2}, & [3\mathrm{D}] \\ \dfrac{\sin\theta}{\bar{c}}\dfrac{b_2(k_1^s,\omega)V_1(k_1^s,\eta,\omega)}{\bar{W}_o(k_1^s,\omega,\bar{Z})}\dfrac{1}{(1-\bar{U}\cos\theta)^2}\dfrac{D_j}{t_o}. & [2\mathrm{D}] \end{array} \right. \tag{63}$$

Here $\bar{W}_o = D_j W_o$ is dimensionless, and derivatives present in the Wronskian are now evaluated with respect to the normalized distance η . Factor (D_j/t_o) present in the 2D solution implies that the pressure field is evaluated per unit flow thickness t_o in x_2 direction. Since the Wronskian in equation (22) is independent of normal distance to the wall, computationally it is advantageous if it were evaluated at infinity where V_2 may be eliminated from the solution

$$\frac{b_2(\vec{k}_t^{\,s},\omega)}{\bar{W}_o(\vec{k}_t^{\,s},\omega,\bar{Z})} = -\left[\frac{e^{iD_j\chi_\infty\eta}}{iD_j\chi_\infty V_1(\vec{k}_t^{\,s},\eta,\omega) + dV_1(\vec{k}_t^{\,s},\eta,\omega)/d\eta}\right]_{\eta\to\infty} . \tag{64}$$

Sample Computations

We start with a rigid boundary condition on the wall ($\overline{Z} \to \infty$) and a set of values for the observer location and flow condition as ($\phi = \pi/2, \theta = \pi/4, St_o = 0.25, U_j/c_\infty = 0.90, T_R = 3.0$). Two linearly independent solutions V_1 and V_2 to equation (22) are shown in figures 8 and 9. Solution V_1 is real, and possesses a relatively larger amplitude compared to the second solution V_2. It is noteworthy that in view of equation (25), the amplitudes of V_1 and V_2 are entirely arbitrary, and the GF should be independent of this selection. At large distance η from the boundary, both V_1 and V_2 exhibit an oscillatory behavior with a regular wavelength of $2\pi/|\chi_\infty|$.

Parameter $b_2(\vec{k}_t^s, \omega)$ is complex, and is determined from Eq. (29) as $\eta \to \infty$. Figure 10 shows that factor $V_2(\eta)\exp(i\eta D_j \chi_\infty)$ approaches constant b_2 shortly after $\eta = 4$. The real and imaginary components of $G_N(\eta, \omega)$ are presented in Fig. 11. It is seen that the zero intersects of G_N follow those of $V_1(\eta)$. It is noted that the GF represents the combined effect of direct radiation from a harmonic point source at η plus reflection from the surface (and the adjacent flow), therefore zero intersect-points correspond to source locations where the two effects cancel each other out. Since the far-field pressure is evaluated according to equation (49) as the convolution of the source correlation function and the GF, the importance of the GF appears primarily within the region of nonzero sources. This, most likely, is limited to the initial several diameters normal to the wall where jet/wall turbulence and/or heat related sources are present. Figure 12 displays an expanded view of the GF within the first 2 diameters normal to the wall. The amplitude is relatively larger at $\eta = 1$ compared to regions within the BL, and the phase is constant at 1.16 *Rad*.

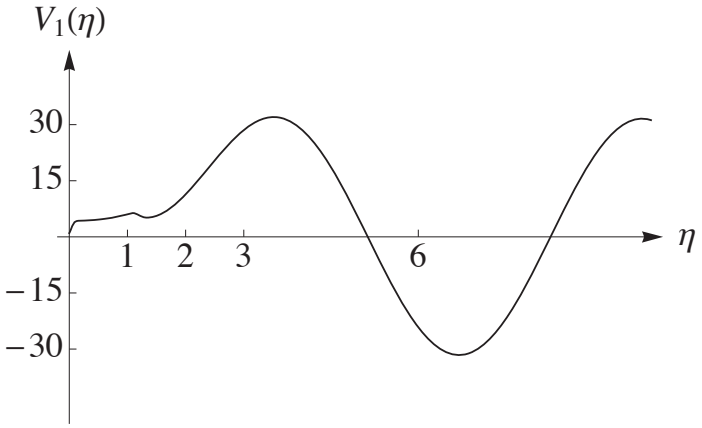

Figure 8. Solution $V_1(\eta)$ subject to the mean velocity and temperature profiles of Fig. 7 at $(\phi = \pi/2, \theta = \pi/4, St_o = 0.25, U_j/c_\infty = 0.90, T_R = 3.0)$.

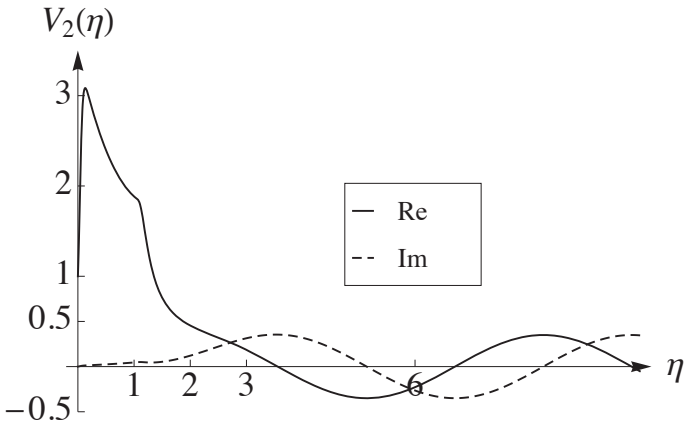

Figure 9. Real (solid line) and imaginary (dashed line) components of solution $V_2(\eta)$ subject to the mean flow profiles of Fig. 7 at $(\phi = \pi/2, \theta = \pi/4, St_o = 0.25, U_j/c_\infty = 0.90, T_R = 3.0)$.

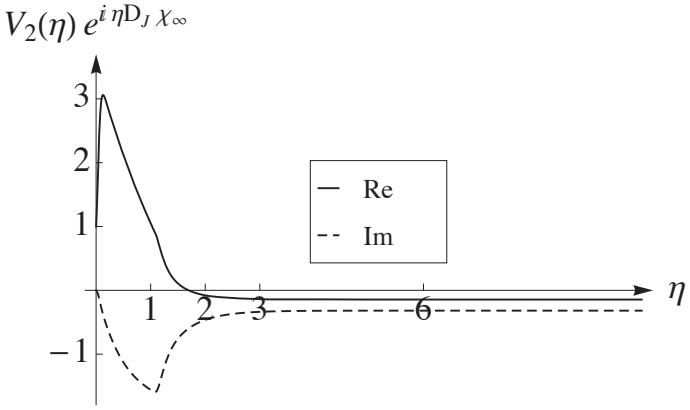

Figure 10. Real (solid line) and imaginary (dashed line) components of constant parameter b_2 as $\eta \to \infty$.

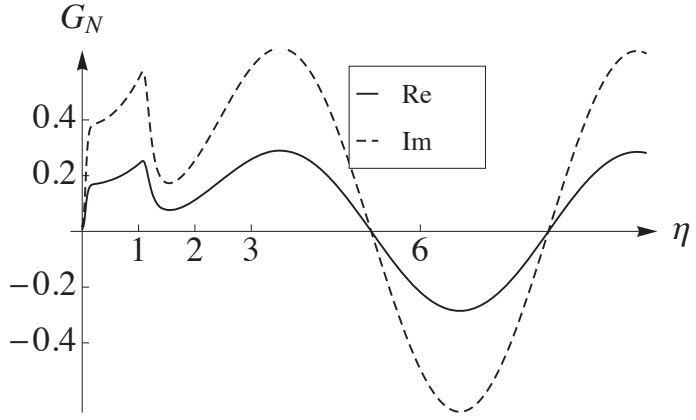

Figure 11. Real (solid line) and imaginary (dashed line) components of the Green's function $G_N(\eta, \omega)$ at $(\phi = \pi/2, \theta = \pi/4, St_o = 0.25, U_j/c_\infty = 0.90, T_R = 3.0)$.

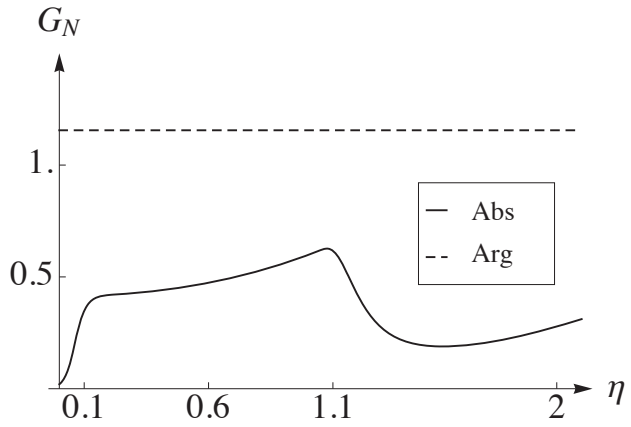

Figure 12. Magnitude (solid line) and phase (dashed line) of the Green's function $G_N(\eta,\omega)$ at $(\phi=\pi/2, \theta=\pi/4, St_o=0.25, U_j/c_\infty=0.90, T_R=3.0)$.

Next, the frequency is increased to $St_o=0.50$ and 1.0, while the remaining parameters are kept the same as before. Noticeable reduction in the magnitude of the GF (see Fig. 13) indicates that sound generation within the region of nonzero sources should decrease at higher source frequency provided that the source density remains constant. In the special case of a uniform mean flow $(U=const, c=const)$, it is readily shown that the two linearly independent solutions to Eq. (22) are $V_1=\cos(x_3\chi)$ and $V_2=\exp(i\,x_3\chi)$, which results in a Wronskian of $W_o=i\chi$. Parameter χ is evaluated according to Eq. (11) with $\vec{k}_t=\vec{k}_t^{\,s}$, and is independent of the normal distance from the surface. Using that in Eq. (42) shows that the GF is inversely proportional to frequency.

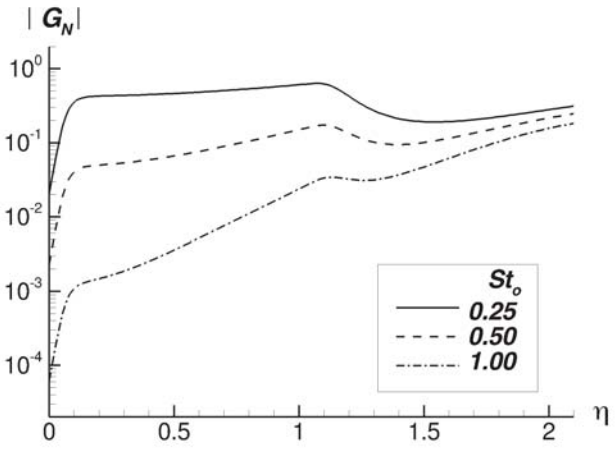

Figure 13. Dependence of the GF magnitude on source frequency $(\phi=\pi/2, \theta=\pi/4, U_j/c_\infty=0.90, T_R=3.0)$.

In the next example, temperature effect is examined at T_R = 1.0 and 2.0, while the remaining parameters are kept the same as in Fig. 12. The temperature profile for the unheated case is shown in Fig. 14. As shown in Fig. 15, the GF magnitude near the wall ($\eta<1.1$) is increased considerably (nearly four times) as the jet temperature ratio is reduced from 3.0 to 1.0. It is noted that according to Eq. (63), that temperature effect enters the computations through factors (c_∞/c) as well as solution $V_1(\eta)$.

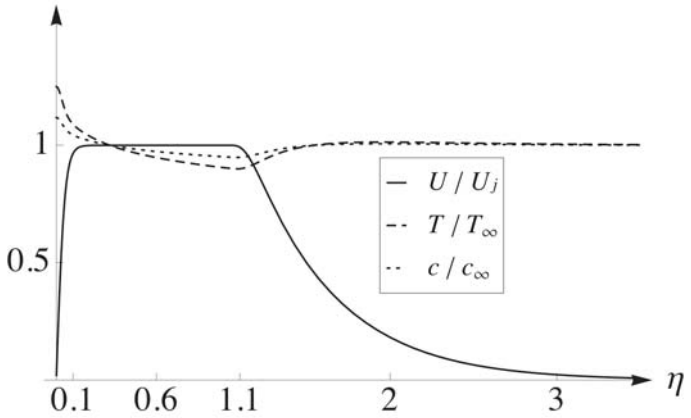

Figure 14. Mean flow profiles for mean axial velocity (solid line), static temperature (dashed line) and sound speed (dotted line) at $U_j / c_\infty = 0.90, T_R = 1.0$ **.**

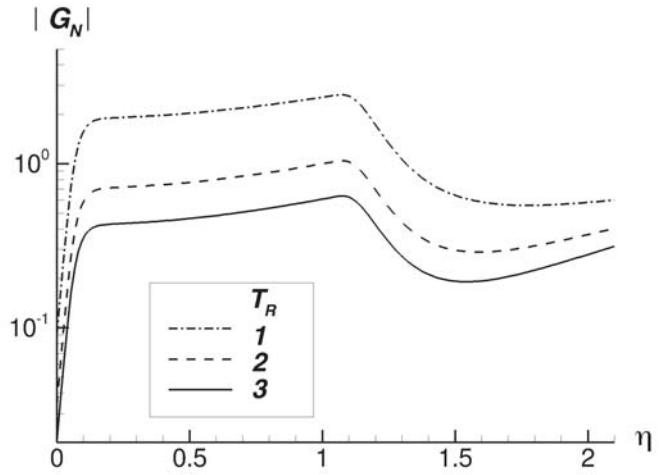

Figure 15. Dependence of the GF magnitude on temperature $(\phi = \pi/2, \theta = \pi/4, St_o = 0.25, U_j / c_\infty = 0.90)$.

The effect of the observer angle on the GF is examined at 3 polar angle of $\theta = 45^o, 90^o$, and 120^o while the remaining parameters stay the same as before. Figure 16 shows a substantial increase in the magnitude of the GF within the BL ($\eta < 0.13$) along the sideline (at 90^o) as well as at up-stream angle of 120^o compared to 45^o.

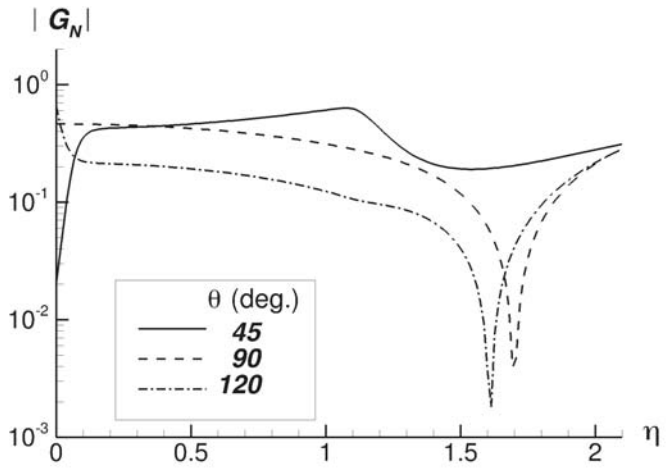

Figure 16. Magnitude of the Green's function G_N at indicated polar angles at $(\phi = \pi/2,\ St_o = 0.25, U_j/c_\infty = 0.90, T_R = 3.0)$.

Wall conditions may be examined by selecting numerical values for the normalized impedance function $\overline{Z}$. The real and imaginary components of the surface impedance depend not only on the wall characteristics (such as resistance and reactance of a liner), but also on the external flow characteristics such as Mach number as well as sound frequency and amplitude [28, 29]. Aside from the solid boundary conditions $(\overline{Z} \to \infty)$ examined earlier, here we choose a pair of values for the specific resistance and reactance as $\overline{Z} = (3.0, 0)$ and $\overline{Z} = (1.0, 0.5)$. Computational results are shown in figure 17 at unheated condition $T_R = 1.0$. At an observer angle of $\theta = \pi/4$, the amplitude of the GF is rather unaffected between $\overline{Z} = \infty$, and 3.0, and is slightly reduced at $\overline{Z} = (1.0, 0.5)$. The phase (shown in radians) is constant for the rigid wall, but becomes a function of the source location with a non-rigid type boundary condition.

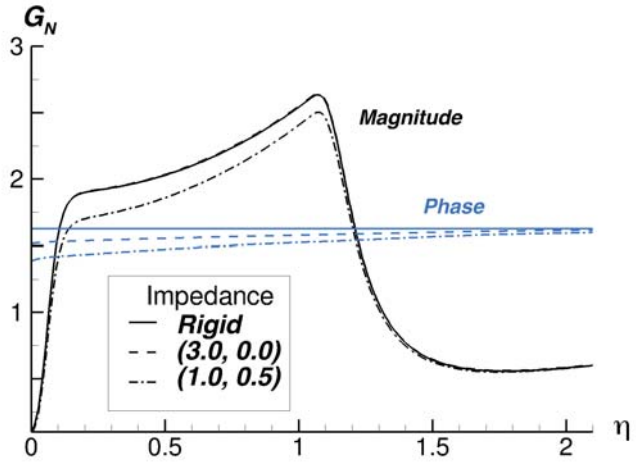

Figure 17. The effect of wall impedance on the GF – rigid wall: (solid line); $\overline{Z} = (3.0, 0.0)$: (dashed line); $\overline{Z} = (1.0, 0.5)$: (dash-dot); $(\phi = \pi/2, \theta = \pi/4, St_o = 0.25, U_j/c_\infty = 0.90, T_R = 1.0)$.

Flight effects are examined for a range of polar angles θ at a constant azimuthal angle of $\phi=\pi/2$ using selective ambient Mach numbers of 0.0, 0.20 and 0.35. The 2D and 3D solutions scale differently with respect to flight factor. Using equations (42) and (58a), it is readily shown that the two GF solutions scale as $(1-M_\infty^2\sin\theta)^{-1}$ and $(1-M_\infty^2\sin\theta)^{-3/4}$ at $\phi=\pi/2$, respectively. Here we choose the 3D solution to investigate the flight effects. The remaining parameters are selected as $St_o=0.25, U_j/c_\infty=0.90, T_R=1.0,$ and $\bar{Z}\to\infty$. Shown in figure 18 is the GF at the ambient Mach numbers of $M_\infty=0.0$ and 0.35 as evaluated following Eq. (42). It is seen that the peak directivity angle rotates from $\theta=57^o$ under static condition to $\theta=35^o$ in flight at $M_\infty=0.35$. Aside from source location, directivity pattern is a function of frequency and jet temperature.

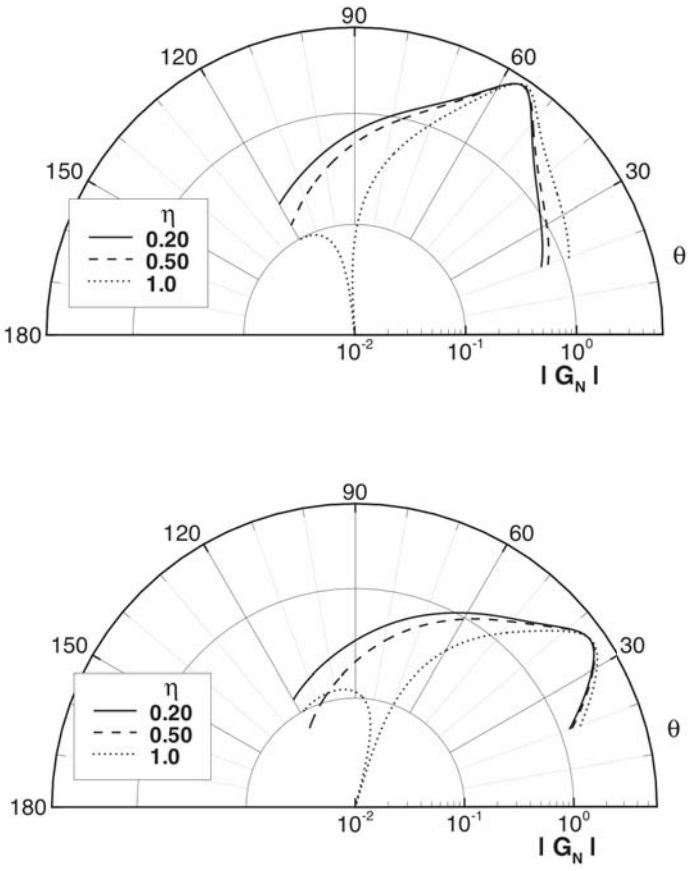

Figure 18. **GF directivity for indicated source ($\eta=0.20,0.50,1.0$) at $M_\infty=0.0$ (top); and $M_\infty=0.35$ (bottom), with ($St_o=0.25, U_j/c_\infty=0.90, T_R=1.0, \phi=\pi/2$).**

Finally, we examine the above GF in a high-aspect ratio rectangular jet in isolation (in absence of a surface). Since the GF accounts for both the wall reflection and direct radiation from the source, we should expect a reduction in the magnitude of G_N in absence of a reflecting wall – although the shear layer itself could refract the sound in certain directions. The mean velocity selected for this exercise (see Fig. 19) exhibits a decay profile similar to that presented earlier in figure 14, and the static temperature is evaluated according to Crocco-Busemann law (61a) at a stagnation temperature ratio of $T_R=1.0$. The corresponding Green's function is readily evaluated as discussed in Appendix

D. A sample result is shown in figure 20 relative to a far-field observer positioned on the positive side ($+x_3$), and at a polar angle of 45°. Significant noise shielding is achieved when the source is located outside the shear layer on the opposite side of the observer (such as $\eta = -3$). When the source is outside the shear layer but on the same side as the observer, the shielding represents a periodic pattern (standing-wave) due to direct radiation plus refraction from the shear layer. Within the jet plume or its shear layer, sources more distant from the observer are subject to more shielding, i.e., smaller GF.

The polar directivity of the GF in an isolated jet is further examined when a point source at $St_o = 0.25$ is placed on the centerline ($\eta = 0$). This is compared (see figure 21) with the earlier directivity predictions in the presence of a rigid wall at source locations of ($\eta = 0.20$ and 0.50). An increase of 5-6 dB is predicted with surface present. In the absence of a source model, we *qualitatively* compare this last result with measurements [4] in an AR=8 rectangular jet, with thickness D_j = 0.6696-in normal to surface, plate length X_{TE} =12.0-in, and standoff h =0. The nozzle operating condition is set point SP07 (Mach 0.97, $T_R = 1.0$, $U_j / c_\infty = 0.90$). At $f = 5000\text{-}Hz$, corresponding to Strouhal frequency of $f D_j / U_j = 0.28$, jet noise directivity measurements (figure 22) project a similar increase in noise above the surface as that predicted by the GF calculations shown in figure 21.

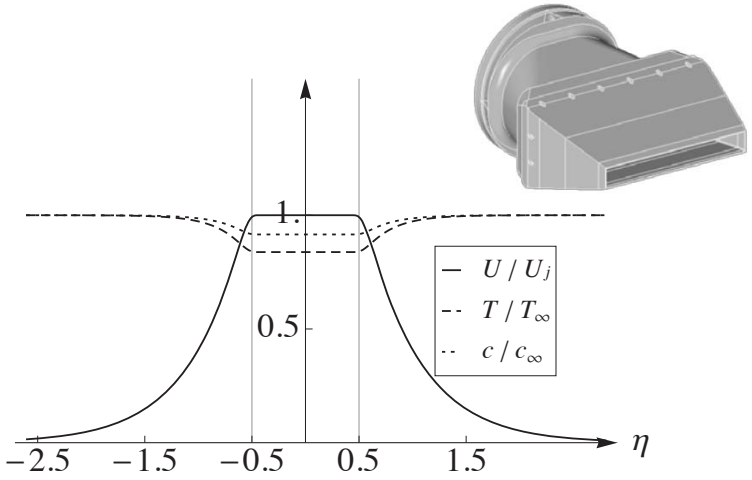

Figure 19. Mean flow profiles in the absence of a nearby surface: mean axial velocity (solid line), static temperature (dashed line) and sound speed (dotted line), at $U_j / c_\infty = 0.90, T_R = 1.0$.

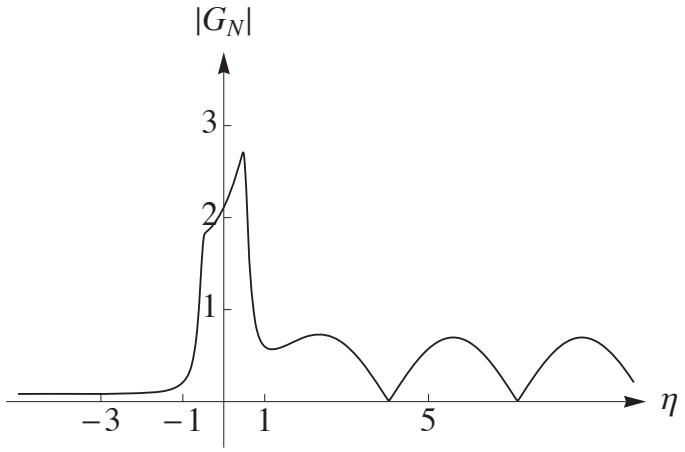

Figure 20. Green's function $G_N(\eta,\omega)$ in an isolated rectangular jet with an observer at ($x_3 \to +\infty$), and $(\phi = \pi/2, \theta = \pi/4, St_o = 0.25, U_j/c_\infty = 0.90, T_R = 1.0)$.

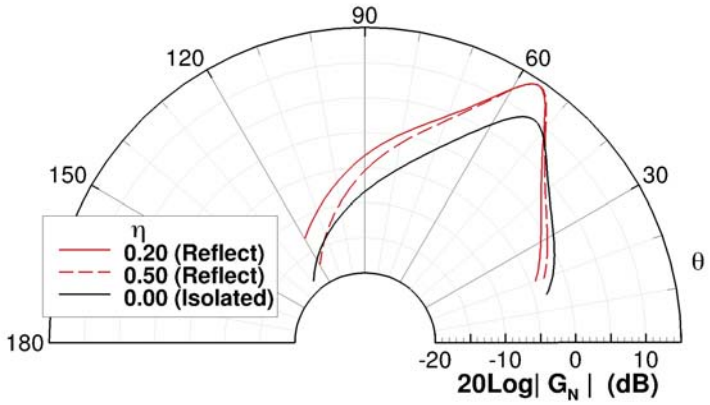

Figure 21. Green's function directivity in a high AR rectangular jet, with/without a rigid surface, at indicated source locations with $(\phi = \pi/2, St_o = 0.25, U_j/c_\infty = 0.90, T_R = 1.0)$.

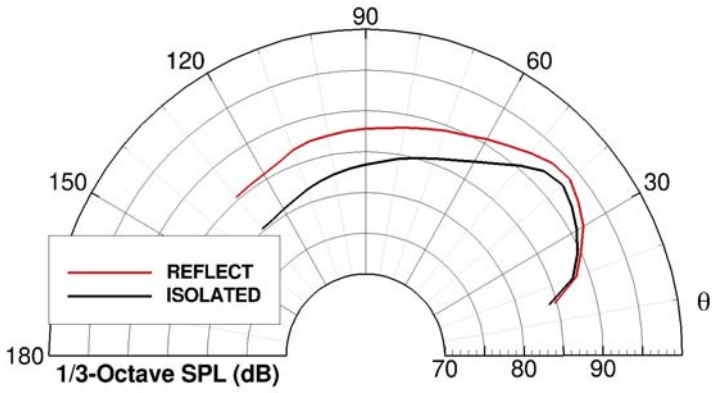

Figure 22. Measured SPL directivity [Ref. 4] at a center frequency of 5000-Hz, AR= 8 rectangular exhaust with $(X_{TE} = 12.0\text{–in.}, h = 0)$ and jet condition SP07 $(U_j/c_\infty = 0.90, T_R = 1.0)$.

7.0 Summary

Prediction of the aircraft noise due to the interaction of the jet exhaust with a nearby solid surface is of increasing interest in the design of future civil transport. Concepts such as hybrid wing body aircraft, over the wing engine mount, or distributed propulsion are likely to contribute to jet surface interaction noise. While nearby surfaces could provide significant noise shielding in certain directions, they also increase noise in other directions. In this study, we presented a formal solution to the propagation Green's function applicable to a rectangular jet exhaust in the proximity of a flat surface. The governing equation is the compressible Pridmore-Brown equation. Both frictional heat generation and thermal gradients in the boundary layer are potential contributors to noise generation and propagation. The general expression for the far-field noise (Eq. 49) resembles that in the absence of a nearby surface – the major difference is concealed in the propagator, which should now be evaluated subject to prescribed boundary conditions on the surface. It was pointed out that aside from the scrubbing noise, scattered noise (or trailing edge noise) is also present on both side of the surface. A comprehensive prediction model needs to account for both noise components.

Using analytical representations of the mean flow profiles, results were presented that show a parametric study of the propagation Green's function at selective values of the source frequency, jet temperature, observer angle, wall impedance, and flight Mach number. It was shown that the magnitude of the GF decreases with increasing source frequency and/or jet mean temperature. The phase remains constant for a rigid surface, but varies with source location subject to a non-rigid surface. As expected, presence of an ambient Mach number sways the peak directivity angle to smaller downstream angles. Absence of a reflecting wall reduced the impact of the GF on the noise level by 5 to 6-dB.

For round jets, a conformal mapping to a rectangular strip needs to be carried out. In practice, a Reynolds-Averaged Navier-Stokes solution to the nozzle flow in the proximity of the surface (with an appropriate turbulence model) provides the mean flow and turbulence information required for modeling both momentum-flux and enthalpy-flux source components. The propagation equation should be solved numerically at each pair of observer angles (θ, ϕ), and at each frequency ω subject to the *local* mean velocity and density profiles. In a 2D formulation, the GF is evaluated according to Eq. (58) while the mean flow is considered as a superposition of parallel slices in x_1 direction and infinitely long in x_2 direction. When the locally parallel flow approximation is extended to x_2 direction the GF is evaluated according to Eq. (42). Here, the jet may be sub-divided into elements in the span-wise x_2 direction in order to account for a finite wetted domain with an eventual decay of the source density in this direction.

Nomenclature

b_2	Far-field amplitude (eq. 29)
c	Sound speed
χ	Phase (eq. 11)
D_j	Jet dimension
δ_o	Boundary layer thickness
η	Normalized distance y_3 / D_j
G	Green's function
$\hat{G}, \breve{G}$	Transformed Green's function
G_N	Normalized Green's function
h'	Enthalpy fluctuations
h	Enthalpy
h'_o	Moving frame stagnation enthalpy ($h' + v'_j v'_j / 2$)
γ	Specific heats ratio
Γ	Source

$\vec{k}$	Wave number
$\vec{k}_t$	Wave number vector (k_1, k_2)
κ_o	Wave number magnitude (ω / c_∞)
M	Mach number (U / c)
ω	Radian frequency $(2\pi f)$
π'	Normalized pressure fluctuation
p'	Acoustic pressure
$P(k_t, \omega)$	Wall-pressure wave number-frequency spectrum
$q(\vec{y}, \vec{\xi}, \tau)$	Source correlation function
ρ	Density
R	Distance $\lvert\vec{x} - \vec{y}\rvert$
St_o	Strouhal frequency $f D_j / U_j$
$\vec{\xi}$	Spatial separation vector
ψ	Wall function (eq. 21b)
t	Time
T_R	Stagnation temperature ratio
τ	Time delay
U	Mean axial velocity
U_e	Peak velocity in the boundary layer
v_i'	Fluctuating velocity component
$\tilde{v}_i$	Mass-averaged velocity component
θ	Polar angle
ϕ	Azimuthal angle
W_o	Wronskian
$\vec{x}$	Rectangular coordinates
$\vec{y}$	Source location
$\bar{Z}$	Normalized surface impedance

Subscripts

o	At the surface variable
∞	At ambient conditions

Superscripts

–	Time average
^	Fourier transformed variable
~	Favre average $(\tilde{q} = \overline{\rho q} / \bar{\rho})$

Appendix-A Influence of the Solid Surfaces

By dividing the flow variables into their mean and fluctuating components, the Navier-Stokes equations may be rewritten as a set of mean flow equations, plus a set of five linear equations for the fluctuating components [18]

$$L_{\nu\mu}u_{\mu} = f_{\nu}(\vec{x},t)\,, \qquad (\mu,\nu = 1,2,...,5) \tag{A1}$$

where u_{μ} denotes the five dependent fluctuating variables

$$\begin{aligned} u_{\mu} &= (m_i, p'_e, \rho') \\ m_i &= \rho v'_i, \quad i = 1,2,3 \end{aligned} \tag{A2}$$

(Latin indices repeat from 1 to 3, and Greek indices repeat from 1 to 5). The first three equations in (A1) correspond to the linearized momentum equation, followed by the energy and mass equations in the fourth and fifth place. The source term appearing on the right hand side of (A1) is

$$f_{\nu}(\vec{x},t) = \frac{\partial}{\partial x_j}e''_{\nu j} + \delta_{\nu 4}(\gamma-1)e''_{ij}\frac{\partial \tilde{v}_i}{\partial x_j}, \quad (i,j = 1,2,3), \quad \nu = 1,\ldots,5 \tag{A3}$$

$$\begin{aligned} e''_{\nu j} &= -(\rho v'_{\nu}v'_j - \overline{\rho v'_{\nu}v'_j}), \\ v'_4 &= (\gamma-1)(h' + \frac{1}{2}v'^2), \quad v'_5 = 0\,. \end{aligned} \tag{A4}$$

The first three source components relate to difference between momentum flux terms and their Favre-averaged values, while the fourth term is related to the enthalpy flux and its Favre-averaged value, and the fifth source term (mass equation) is obviously zero.

Note that both momentum variable m_i and pressure variable p'_e are non-linear, however, in practice we set $m_i \simeq \bar{\rho}v'_i$, and

$$p'_e = p' - \frac{(\gamma-1)}{2}e''_{kk}\,, \tag{A5}$$

implies that $p'_e \simeq p'$ in the acoustic domain where turbulence is zero.

The Green's Function (GF) to set of equations (A1) with a non-zero delta function source placed in the σth equation is denoted as $g_{\mu\sigma}$

$$L_{\nu\mu}g_{\mu\sigma}(\vec{x},t\,|\,\vec{y},\tau) = \delta_{\nu\sigma}\delta(\vec{x}-\vec{y})\delta(t-\tau). \tag{A6}$$

The field variables of interest are obtained from equations (A1) and (A6) using the source/GF convolution integral

$$u_{\mu}(\vec{x},t) = \int_{\tau}\int_{\vec{y}} g_{\mu\nu}(\vec{x},t\,|\,\vec{y},\tau)f_{\nu}(\vec{y},\tau)d\vec{y}d\tau\,, \tag{A7}$$

For example, when $\mu = 4$ the far-field acoustic pressure is evaluated as

$$p'(\vec{x},t) \approx p'_e(\vec{x},t) = \int_{\tau}\int_{\vec{y}} g_{4\nu}(\vec{x},t \mid \vec{y},\tau) f_\nu(\vec{y},\tau) d\vec{y} d\tau \ . \tag{A8}$$

Considering that $f_5 = 0$, the latter operation requires solving (A6) four times, each time by placing a delta function in the one of the first four equations. This process would also solve for other GF components that are not necessary for evaluating p'. It is computationally advantageous if the field variables were evaluated from the set of the adjoint equations that are governed by

$$L^{(a)}_{\nu\mu}\ g^{(a)}_{\mu\sigma}(\vec{x},t \mid \vec{y},\tau) = \delta_{\nu\sigma}\delta(\vec{x}-\vec{y})\delta(t-\tau)\,. \tag{A9}$$

The adjoint operator (denoted by superscript *a*) is readily evaluated once we multiply equation (A1) by $g^{(a)}_{\nu\sigma}(\vec{x},t \mid \vec{y},\tau)$, and rearrange its right hand side to appear as

$$g^{(a)}_{\nu\sigma}(\vec{x},t \mid \vec{y},\tau) L_{\nu\mu} u_\mu(\vec{x},t) = u_\mu(\vec{x},t) L^{(a)}_{\mu\nu}\, g^{(a)}_{\nu\sigma}(\vec{x},t \mid \vec{y},\tau) + \frac{\partial}{\partial t}\left(u_\mu g^{(a)}_{\mu\sigma}\right) + \frac{\partial}{\partial x_j} F_{j\sigma}\,. \tag{A10}$$

The last two terms on the RHS of (A10) represent the bi-linear form of u_μ and $g^{(a)}_{\mu\sigma}$, and

$$F_{j\sigma}(\vec{x},t \mid \vec{y},\tau) = \tilde{v}_j(\vec{x},t) u_\mu(\vec{x},t) g^{(a)}_{\mu\sigma}(\vec{x},t \mid \vec{y},\tau) + u_4 g^{(a)}_{j\sigma} + u_j\left(g^{(a)}_{5\sigma} + c^2 g^{(a)}_{4\sigma}\right). \tag{A11}$$

We solve for $u_\sigma(\vec{y},\tau)$ by placing (A9) into (A10), and integrating this equation within a large four-dimensional space-time volume $(\vec{x},t)$ surrounding the source

$$\int_t\int_{\vec{x}} g^{(a)}_{\nu\sigma}(\vec{x},t \mid \vec{y},\tau) f_\nu(\vec{x},t)\, d\vec{x}\, dt = u_\sigma(\vec{y},\tau) + \int_t\int_{\vec{x}}\left(\frac{\partial}{\partial t}\left(u_\mu g^{(a)}_{\mu\sigma}\right) + \frac{\partial}{\partial x_j} F_{j\sigma}\right) d\vec{x} dt\,. \tag{A12}$$

Following the divergence theorem, the volume integral on the RHS of (A12) may be converted into a surface integral. When there are no solid surfaces present to interfere with the sound, this integral is evaluated on the surface of a large 4D sphere in $(\vec{x},t)$ domain – resulting in a null contribution due to the vanishing of the field variables u_μ on such a surface. Consequently (A12) becomes

$$u_\mu(\vec{x},t) = \int_{\tau}\int_{\vec{y}} g^{(a)}_{\nu\mu}(\vec{y},\tau \mid \vec{x},t) f_\nu(\vec{y},\tau) d\vec{y} d\tau\,. \qquad \text{(No solid surfaces)} \tag{A13}$$

Equations (A7) and (A13) point to the reciprocity of the GF in the absence of solid surfaces, i.e.,

$$g^{(a)}_{\nu\mu}(\vec{y},\tau \mid \vec{x},t) = g_{\mu\nu}(\vec{x},t \mid \vec{y},\tau)\,. \tag{A14}$$

By setting $\mu = 4$ we evaluate the far-field pressure. It is seen that the advantage of (A13) over (A7) is that we now place a source only in the fourth equation within set (A9) to compute the required GF components for pressure. Equation (A13) represents the fundamental solution to the governing equations. In the presence of solid boundaries in a finite domain, the general solution, when formulated in terms of the adjoint GF, is complemented with surface integrals as shown in (A12). The reciprocity condition (A14) would not necessarily be satisfied when reflecting boundaries are present in the acoustic medium unless surface integrals are forced to disappear by imposing conditions on the adjoint GF.

To investigate the surface integrals further, we allow volume $\vec{x}(t)$, externally and/or internally, be bounded by surface $s(t)$ with a unit outward normal $\vec{n}$ (Fig. A1). The first term within the bracket on the RHS of (A12) is expressed as the sum of two terms following the Leibniz's rule

$$\int_{\vec{x}(t)} \frac{\partial}{\partial t}\left(u_\mu g^{(a)}_{\mu\sigma}(\vec{x},t\,|\,\vec{y},\tau)\right)d\vec{x} = \frac{d}{dt}\int_{\vec{x}(t)} u_\mu g^{(a)}_{\mu\sigma}(\vec{x},t\,|\,\vec{y},\tau)d\vec{x} - \int_{s(t)} \vec{n}\cdot\vec{V}^s u_\mu g^{(a)}_{\mu\sigma}(\vec{x},t\,|\,\vec{y},\tau)ds \ , \quad \text{(A15)}$$

where $\vec{V}^s(\vec{x},t)$ is the velocity at an arbitrary point on the surface $s(t)$. We now integrate both sides of (A15) within the time interval [-T, T] for some large time T. The first terms on the RHS of (A15) vanishes due to the initial condition (in a remote past time), and the causality condition. Inserting (A15) into (A12) and applying the divergence theorem to the last term in (A12), we find (upon interchanging dummy variables)

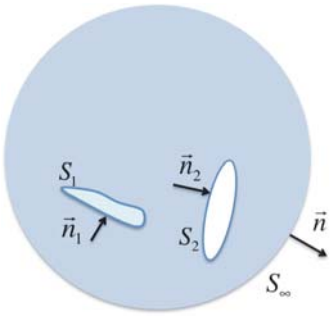

Figure A1. Solid surfaces within the acoustic medium.

$$u_\mu(\vec{x},t) = \int_\tau\int_{\vec{y}} g^{(a)}_{\nu\mu}(\vec{y},\tau\,|\,\vec{x},t)f_\nu(\vec{y},\tau)d\vec{y}d\tau + \int_{-T}^{T} d\tau \int_{s(\tau)} n_j\left[V^s_j u_\nu g^{(a)}_{\nu\mu}(s,\tau\,|\,\vec{x},t) - F_{j\mu}(s,\tau\,|\,\vec{x},t)\right]ds. \quad \text{(A16)}$$

Integral equation (A16) represents a formal solution to the problem. The two integrals represent contributions to the acoustic field due to the volume and surface sources, respectively. In particular, the acoustic pressure is solved when $\mu = 4$. Moving the partial derivatives from source to the GF and/or imposing boundary conditions on the surface integrals may achieve further simplifications. For example, placing f_ν from (A3) into (A16), and using the identity

$$g^{(a)}_{\nu\mu}(\vec{y},\tau\,|\,\vec{x},t)\frac{\partial}{\partial y_j}e''_{\nu j} = \frac{\partial}{\partial y_j}\left(g^{(a)}_{\nu\mu}(\vec{y},\tau\,|\,\vec{x},t)e''_{\nu j}\right) - e''_{\nu j}\frac{\partial}{\partial y_j}g^{(a)}_{\nu\mu}(\vec{y},\tau\,|\,\vec{x},t),$$

followed by application of the divergence theorem on the first term on the right shows that

$$\begin{aligned} u_\mu(\vec{x},t) = &-\int_\tau\int_{\vec{y}}\left(\frac{\partial g^{(a)}_{\nu\mu}}{\partial y_j} - (\gamma-1)\frac{\partial \tilde{v}_\nu}{\partial y_j}g^{(a)}_{4\mu}\right)e''_{\nu j}(\vec{y},\tau)d\vec{y}d\tau + \int_{-T}^{T} d\tau\int_s n_j g^{(a)}_{\nu\mu}(s,\tau\,|\,\vec{x},t)e''_{\nu j}dsd\tau \\ &+ \int_{-T}^{T} d\tau\int_s n_j\left[V^s_j u_\nu g^{(a)}_{\nu\mu}(s,\tau\,|\,\vec{x},t) - F_{j\mu}(s,\tau\,|\,\vec{x},t)\right]ds. \end{aligned} \quad \text{(A17)}$$

Further, substituting for $F_{j\mu}$ from (A11) into this last expression and imposing the no-slip boundary condition on the surface, $(V^s_j - \tilde{v}_j).n_j = 0$, results in the following integral equation for pressure

$$\begin{aligned} p'_e(\vec{x},t) = &-\int_\tau\int_{\vec{y}}\Gamma^{(a)}_{\nu j}(\vec{y},\tau\,|\,\vec{x},t)e''_{\nu j}(\vec{y},t)d\vec{y}d\tau + \int_{-T}^{T} d\tau\int_s n_j g^{(a)}_{\nu 4}(s,\tau\,|\,\vec{x},t)e''_{\nu j}ds \\ &- \int_{-T}^{T} d\tau\int_s n_j\left[p'_e(s,\tau)g^{(a)}_{j4}(s,\tau\,|\,\vec{x},t) + m_j(s,\tau)(g^{(a)}_{54} + c^2 g^{(a)}_{44})\right]ds, \end{aligned} \quad \text{(A18)}$$

where

$$\Gamma_{\nu j}^{(a)} \equiv \frac{\partial g_{\nu 4}^{(a)}}{\partial y_j} - (\gamma - 1)\frac{\partial \tilde{v}_\nu}{\partial y_j} g_{44}^{(a)} . \tag{A19}$$

Appendix-B Vanishing of the Surface Integrals

Here we show that the boundary condition (21) eliminates the surface integrals in the Green's function formulation of the acoustic field for bounded media. We start with equation (1), and apply Fourier transform with respect to variables x_1, x_2 and t as defined in Eq. (7) with the over hat carrot denoting a transformed variable

$$\frac{\partial^2 \hat{\vartheta}}{\partial x_3^2} + f(\vec{k}_t, x_3, \omega)\hat{\vartheta} = \hat{\Lambda}, \tag{B1}$$

where function f was defined in Eq. (11) and

$$\hat{\vartheta}(\vec{k}, x_3, \omega) \equiv \hat{\pi}'(\vec{k}_t, x_3, \omega)\frac{c(x_3)}{-\omega + k_1 U(x_3)}, \quad \hat{\Lambda}(\vec{k}, x_3, \omega) \equiv \frac{i\hat{\Gamma}}{c(x_3)\left(-\omega + k_1 U(x_3)\right)^2}. \tag{B2}$$

Multiply Eq. (9) by $\hat{\vartheta}$, and equation (B1) by $\breve{G}$, subtract the two expressions, and integrate the result with respect to x_3

$$\int_0^\infty \left(\breve{G}\frac{\partial^2 \hat{\vartheta}}{\partial x_3^2} - \hat{\vartheta}\frac{\partial^2 \breve{G}}{\partial x_3^2} \right) dx_3 = \int_0^\infty \left(\breve{G}\hat{\Lambda} - \hat{\vartheta}\,\delta(x_3 - y_3) \right) dx_3, \tag{B3}$$

or

$$-\left(\breve{G}\frac{\partial \hat{\vartheta}}{\partial x_3} - \hat{\vartheta}\frac{\partial \breve{G}}{\partial x_3} \right)\Bigg|_0^\infty = \hat{\vartheta}(\vec{k}, y_3, \omega) - \int_0^\infty \breve{G}(\vec{k}_t, x_3 \mid y_3, \omega)\hat{\Lambda}(\vec{k}, x_3, \omega) dx_3 . \tag{B4}$$

Upon recognizing that $\partial\hat{\vartheta}/\partial x_3 = -i\chi_\infty \hat{\vartheta}$, and $\partial\breve{G}/\partial x_3 = -i\chi_\infty \breve{G}$ at infinity, the upper limit of the expression on the left hand side of (B4) vanishes. On the right, since the GF is self-adjoint we switch x_3 and y_3 in the argument of $\breve{G}$, and subsequently we substitute expressions for $\hat{\Lambda}$ from (B2), and $\breve{G}$ from (10) into (B4) to show that in view of (19), the right hand side of this equation also vanishes.

Consequently we arrive at

$$\breve{G}\frac{\partial \hat{\vartheta}}{\partial x_3} - \hat{\vartheta}\frac{\partial \breve{G}}{\partial x_3} = 0, \quad x_3 = 0 . \tag{B5}$$

Using surface boundary condition (18) in (B5) shows that

$$\frac{\partial \breve{G}}{\partial x_3} - \psi \breve{G} = 0, \qquad x_3 = 0 \tag{B6}$$

where function $\psi(k_1, \omega, \bar{Z})$ is given in (21b).

Appendix-C Flight Effect Parameters

Coefficients A_i in equation (44) depend on the observer angles (θ, ϕ), stationary point angles (θ^s, ϕ^s), and flight Mach number M_∞ as

$$A_1 = \sin\phi\cos\theta\sin\phi^s\cos\theta^s + \sin\phi\sin\theta\frac{\partial^2 S}{\partial\theta^{s2}}$$

$$A_2 = \sin\phi\cos\theta\sin\phi^s\cos\theta^s + \cos\phi\cos\phi^s + \sin\phi\sin\theta\frac{\partial^2 S}{\partial\phi^{s2}} \qquad \text{(C1)}$$

$$A_3 = \sin\phi\cos\theta\cos\phi^s\sin\theta^s + \sin\phi\sin\theta\frac{\partial^2 S}{\partial\theta^s\,\partial\phi^s}$$

where

$$\frac{\partial^2 S}{\partial\theta^{s2}} = \frac{1}{S(\theta^s,\phi^s,M_\infty)}\left(-(\frac{\partial S}{\partial\theta^s})^2 + (1-M_\infty^2)\cos 2\theta^s\sin^2\phi^s + M_\infty\cos\theta^s\sin\phi^s\right)$$

$$\frac{\partial^2 S}{\partial\phi^{s2}} = \frac{1}{S(\theta^s,\phi^s,M_\infty)}\left(-(\frac{\partial S}{\partial\phi^s})^2 + (\sin^2\theta^s + M_\infty^2\cos^2\theta^s)\cos 2\phi^s + M_\infty\cos\theta^s\sin\phi^s\right) \qquad \text{(C2)}$$

$$\frac{\partial^2 S}{\partial\theta^s\,\partial\phi^s} = \frac{1}{S(\theta^s,\phi^s,M_\infty)}\left(-\frac{\partial S}{\partial\theta^s}\frac{\partial S}{\partial\phi^s} + \frac{1}{2}(1-M_\infty^2)\sin 2\theta^s\sin 2\phi^s + M_\infty\sin\theta^s\cos\phi^s\right)$$

and

$$\frac{\partial S}{\partial\theta^s} = -\frac{\cos\theta}{\sin\theta}\sin\theta^s\sin\phi^s, \quad \frac{\partial S}{\partial\phi^s} = \frac{\cos\theta}{\sin\theta}\cos\theta^s\cos\phi^s - \frac{\cos\phi}{\sin\theta\sin\phi}\sin\phi^s\ . \qquad \text{(C3)}$$

Parameter $S(\theta^s,\phi^s,M_\infty)$ is evaluated as the negative root of S^2 in equation (35) when $S^2 > 0$.

Appendix-D Green's Function in an Unbounded Medium

In the absence of a boundary surface in the finite domain, the GF expression (42) is still formally applicable to a far-field observer once we recognize that the radiation condition requires $\chi_\infty = \mp\sqrt{\chi_\infty^2}$ as $x_3 \to \pm\infty$ given that $\chi_\infty^2 > 0$. The two boundary points $\pm\infty$ are placed at the two opposite sides of the shear layer, far enough where the mean flow gradients may practically be considered as zero (Fig. D1). As before, the two linearly independent solutions to equation (22) amount to an initial value problem for V_1 and a boundary value problem for V_2. Using notation $\chi_\infty = +\sqrt{\chi_\infty^2}$, we have

$$V_j(x_3) = 1, \quad x_3 \to -\infty, \quad j = 1,2$$

$$\frac{\partial V_j}{\partial x_3} - (-1)^j i\chi_\infty V_j = 0, \quad x_3 \to \begin{vmatrix} -\infty, & j=1 \\ +\infty, & j=2 \end{vmatrix} \qquad \text{(D1)}$$

For an observer at $x_3 \to +\infty$, the GF is evaluated per equation (42), while b_2 is defined according to equation (29).

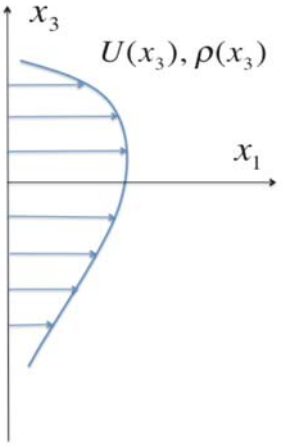

Figure D1. Transversely sheared mean flow in unbounded media.

When the observer is placed at $x_3 \to -\infty$, the GF should be evaluated for $y_3 > x_3$ (see equation 24); subsequently variable $V_2(\vec{k}_t^s, y_3, \omega)$ is used in place of $V_1(\vec{k}_t^s, y_3, \omega)$ in (42), and b_2 is defined as

$$b_2 = V_1(\vec{k}_t^s, x_3, \omega)e^{-i\chi_\infty x_3}, \quad x_3 \to -\infty \qquad \text{(D2)}$$

Acknowledgements

This work was sponsored by the Fixed Wing Project in the NASA Fundamental Aeronautics Program. The author is grateful to the Acoustics Branch at NASA Glenn Research Center for supporting this research effort, and to Drs. S. J. Leib and J. E. Bridges for their perceptive comments and suggestions.

References

[1] *ICAO Environmental Report*, http://cfapp.icao.int/Environmental-Report-2013/index.html#66, (2013).

[2] Brown, C. A., "Jet-Surface interaction test: far-field noise results," ASME paper GT2012-69639, June 2012.

[3] Podboy, G. G., "Jet-Surface interaction test: phased array noise source localization results," ASME paper GT2012-69801, June 2012.

[4] Bridges, J., "Noise from aft deck exhaust nozzles – differences in experimental embodiments," AIAA paper AIAA-2014-0876, January 2014.

[5] FFowcs Williams, J. E., and Hall, L. H., "Aerodynamic sound generation by turbulent flow in the vicinity of a scattering half plane," J. Fluid Mechanics, **40(4)**, (1970), pp. 657–670.

[6] Powell, Alan, "On the aerodynamic noise of a rigid flat plate moving at zero incidence," J. Acoustical Soc. Am., **31(12)**, (1959), pp. 1649-1653.

[7] Lawrence, J. L. T., Azarpeyvand, M., and Self, R. H., "Interaction between a flat plate and a circular subsonic jet, " AIAA paper AIAA-2011-2745, June 2011.

[8] Bowman, J. J., Senior, T. B. A., and Uslenghi, P. L. E., *Electromagnetic and Acoustic Scattering by Simple Shapes* (1987), Hemisphere Publishing Corp., New York.

[9] Howe, M. S., "A review of the theory of trailing edge noise," J. Sound and Vib. **61(3)**, (1978), pp. 437-465.

[10] Goldstein, M. E., "Scattering and distortion of the unsteady motion on transversely sheared mean flows," J. Fluid Mechanics, **91(4)**, (1979), pp. 601-632.

[11] Goldstein, M. E., Afsar, M. Z., and Leib, S. J., "Non-homogeneous rapid distortion theory on transversely sheared mean flows," J. Fluid Mechanics, **736**, (2013), pp. 532-569.

[12] Howe, M. S., "Surface pressure and sound produced by turbulent flow over smooth and rough walls," J. Acoustical Soc. Am., **90(2)**, (1991), pp. 1041-1047.

[13] Sevik, M. M., "Topics in hydrodynamics," *Proceedings of IUTAM Symposium*, Aero- and Hydrodynamics, Lyon (1985), Berlin: Springer-Verlag.

[14] Goldstein, M. E., "Relation between the generalized acoustic analogy and Lilley's contribution to aeroacoustics," International J. Aeroacoustics, **9(4, 5)**, (2010), pp. 401-418.

[15] Pridmore-Brown, D. C., "Sound propagation in a fluid flowing through an attenuating duct," J. Fluid Mech. **4**, (1958), pp. 393–406.

[16] Chase, D. M., and Noiseux, C. F., "Turbulent wall pressure at low wavenumbers: Relation to nonlinear source in planar and cylindrical flow," J. Acoust. Soc. Am., **72(3)**, (1982), pp. 975–982.

[17] Bark, F. H., "On the wave structure of the wall region of a turbulent boundary layer," J. Fluid Mechanics, **70**, (1975), pp. 229–250.

[18] Goldstein, M. E., "A generalized acoustic analogy," J. Fluid Mechanics, **488**, (2003), pp. 313-333.

[19] Chandiramani, K. L. "Diffraction of evanescent waves, with application to aerodynamically scattered sound and radiation from unbaffled planes," J. Acoustical Soc. Am. **55(1)**, (1974), pp. 19-29.

[20] Howe, M. S., "The displacement-thickness theory of trailing edge noise," J. Sound and Vib. **75(2)**, (1981), pp. 239-250.

[21] Jones, D. S., "The scattering of sound by a simple shear layer," Proc. Roy Soc. **A, 284**, (1977), pp. 287–328.

[22] Erdelyi, A., *Asymptotic Expansions* (2010), Dover Publications, Inc.

[23] Khavaran, A., Kenzakowski, D. C., and Mielke-Fagan, A. F., "Hot jets and sources of jet noise," International J. Aeroacoustics, **9(4, 5)**, (2010), pp. 491-532.

[24] Howe, M. S., "On the generation of sound by turbulent boundary layer flow over a rough wall," Proc. R. Soc. London, **A 395**, (1984), pp. 247-163

[25] FFowcs Williams, J. E., "Boundary layer pressure and the Corcos model: A development to incorporate low wavenumber constraints," J. Fluid Mechanics, **125**, (1982), pp. 9-25.

[26] Chase, D. M., "The character of turbulent wall pressure spectrum at sub-convective wavenumbers and a suggested comprehensive model," J. Sound and Vib. **(112)**, (1987), pp.125-147.

[27] Tennekes, H., and Lumley, J. L., *A First Course in Turbulence* (1972), M.I.T. Press.

[28] Watson, W. R., Tracy, M. B., Jones, M. G., and Parrott, T. L., "Impedance eduction in the presence of shear flow," AIAA paper AIAA-2001-2263, May 2001.

[29] Malmary, C., Carbonne, S., Auregan, Y., and Pagneux, V., "Acoustic impedance measurement with grazing flow," AIAA paper, AIAA-2001-2193, May 2001.